PAPER • OPEN ACCESS

Weak lensing trispectrum and Kurt-spectra

To cite this article: Dipak Munshi *et al* JCAP11(2022)020

View the article online for updates and enhancements.

You may also like

- Modern problems in the physical sciences (Scientific session of the Physical Sciences Division of the Russian Academy of Sciences, 30 November 2011)
- Interplay between neutrino and gravity portals for FIMP dark matter
Marco Chianese, Bowen Fu and Stephen F. King
- Multi-scale invariant fields: estimation and prediction
H Ghasemi, S Rezakhah and N Modarresi

This content was downloaded from IP address 193.60.238.99 on 14/03/2024 at 19:34

Journal of Cosmology and Astroparticle Physics
An IOP and SISSA journal

Weak lensing trispectrum and Kurt-spectra

Dipak Munshi,[a] **Hayden Lee,**[b,c] **Cora Dvorkin**[b] **and Jason D. McEwen**[a,d]

[a]Mullard Space Science Laboratory, University College London, Holmbury St Mary, Dorking, Surrey RH5 6NT, U.K.
[b]Department of Physics, Harvard University, 17 Oxford Street, Cambridge, MA 02138, U.S.A.
[c]Kavli Institute for Cosmological Physics, University of Chicago, Chicago, IL 60637, U.S.A.
[d]The Alan Turing Institute, Euston Road, London NW1 2DB, U.K.

E-mail: d.munshi@ucl.ac.uk, haydenl@uchicago.edu, cdvorkin@g.harvard.edu, jason.mcewen@ucl.ac.uk

Received December 17, 2021
Revised September 15, 2022
Accepted October 17, 2022
Published November 10, 2022

Abstract. We introduce two kurt-spectra to probe fourth-order statistics of weak lensing convergence maps. Using state-of-the-art numerical simulations, we study the shapes of these kurt-spectra as a function of source redshifts and smoothing angular scales. We employ a pseudo-C_ℓ approach to estimate the spectra from realistic convergence maps in the presence of an observational mask and noise for stage-IV large-scale structure surveys. We compare these results against theoretical predictions calculated using the FFTLog formalism, and find that a simple nonlinear clustering model — the hierarchical ansatz — can reproduce the numerical trends for the kurt-spectra in the nonlinear regime. In addition, we provide estimators for beyond fourth-order spectra where no definitive analytical results are available, and present corresponding results from numerical simulations.

Keywords: cosmological perturbation theory, cosmological simulations, weak gravitational lensing

ArXiv ePrint: 2112.05155

© 2022 The Author(s). Published by IOP Publishing Ltd on behalf of Sissa Medialab. Original content from this work may be used under the terms of the Creative Commons Attribution 4.0 licence. Any further distribution of this work must maintain attribution to the author(s) and the title of the work, journal citation and DOI.

https://doi.org/10.1088/1475-7516/2022/11/020

JCAP11(2022)020

Contents

1 Introduction **1**

2 Formalism **3**
- 2.1 Correlators in harmonic space 3
- 2.2 Computational methods 6
- 2.3 Theoretical model for matter trispectrum 7

3 Weak lensing higher-order statistics **9**
- 3.1 Weak lensing trispectrum 9
- 3.2 Kurt-spectra 11

4 Comparison with ray-tracing simulations **12**
- 4.1 Simulation specifications 12
- 4.2 Results and discussion 13
  - 4.2.1 Shapes of Kurt-spectra 13
  - 4.2.2 Observational mask and noise 14
  - 4.2.3 Comparison with theory 16
  - 4.2.4 Beyond fourth order 17
  - 4.2.5 Low-ℓ modes and finite volume corrections 18

5 Conclusions and future prospects **18**

1 Introduction

Despite the huge amount of progress in cosmology in the past few decades, there still remain many outstanding questions. These include the nature of dark matter (DM), the source of the accelerated expansion of the universe, and the physics of the early universe. In addition, the sum of the neutrino masses [1] remains unknown. It is expected that the operational weak lensing surveys, including the Subaru Hyper Suprime-Cam Survey[1] (HSC) [2], the Dark Energy Survey[2] (DES) [3], the Dark Energy Spectroscopic Instrument (DESI)[3] [4], the Prime Focus Spectrograph[4] [5], the Kilo-Degree Survey (KiDS) [6], as well as near-future Stage-IV large-scale structure (LSS) surveys such as *Euclid*[5] [7], the Vera C. Rubin Observatory[6] [8], and the Roman Space Telescope[7] [9, 10], will improve our understanding to many of the questions that cosmology is facing from high-precision measurements of the intervening mass distribution of the universe.

[1] http://www.naoj.org/Projects/HSC/index.html.
[2] https://www.darkenergysurvey.org.
[3] http://desi.lbl.gov.
[4] http://pfs.ipmu.jp.
[5] http://sci.esa.int/euclid.
[6] http://www.lsst.org/llst home.shtml.
[7] https://roman.gsfc.nasa.gov.

JCAP11(2022)020

Weak lensing observations target the low-redshift universe and small scales, where density perturbations are mostly in the nonlinear regime and the statistics are highly non-Gaussian [11]. Hence, unlike the high-redshift cosmic microwave background (CMB) radiation, the power spectrum alone is not sufficient to distill the entire information content of the data. For this reason, many different estimators have been developed to probe higher-order statistics of weak lensing maps [12]. Initial work in this direction focused primarily on analyzing various statistics that are directly related to the bispectrum such as the integrated bispectrum, a skew-spectrum estimator, and a morphological estimator.

With the increase in high-quality data from ongoing surveys, it is now becoming possible to probe statistics beyond the bispectrum, e.g. the trispectrum, which represents the connected contribution to the four-point correlation function in the Fourier (or harmonic) domain [13, 14]. However, detection and characterization of individual trispectral modes (represented by a quadrilateral) remain computationally challenging. To this end, compressed statistics such as the generalization of the skew-spectrum to fourth order — known also as the *kurt-spectra* — were introduced in the context of 21-cm surveys [15, 16]. Two types of such spectra were implemented in [17, 18] and have already been studied in the context of primordial non-Gaussianity (PNG), where the main motivation was to put independent constraints on the two shapes of local non-Gaussianity parameterized by $\tau_{\rm NL}$ and $g_{\rm NL}$ [19–22]. The situation for the gravity-induced trispectrum is very similar in modified gravity theories, where more than one parameter characterizes the gravity-induced trispectrum. The use of the two kurt-spectra can lift the degeneracy and provide an important consistency check for the constraints from lower-point statistics.

Moreover, the kurt-spectra were used to detect the lensing-induced secondary non-Gaussianity; for example, their application to the WMAP 7-year temperature maps resulted in the first direct constraints of the CMB lensing potential power spectrum [23]. Planck used a similar technique for their analysis [24], and the corresponding fourth-order real-space correlation functions were used in the context of CMB secondaries [10] to separate the lensing of the CMB from the Ostriker-Vishniac effect. In real space, these correlation functions were also studied to arbitrary order in the context of gravity-induced non-Gaussianity in the LSS using the standard perturbation theory (SPT) [25, 26], but in the limit of large angular separations [27]. Theoretical modeling of trispectra has attracted more attention recently [28, 29]. Beyond the SPT, the effective field theory (EFT) based approach has been used to model the trispectrum [30, 31], as well as the halo-model [32] and the hierarchical ansatz based approaches [33], which are valid in the quasi-linear and (highly) nonlinear regimes.

In addition to the summary statistics listed above, in recent years a number of novel modeling techniques have gained popularity. These include Bayesian hierarchical modeling, likelihood-free or forward modeling approaches [34–38], as well as wavelet phase harmonics [39] and the scattering transform [40–42] (see also [43–46] for other works applying scattering transform-type statistics to different astrophysical observables).[8]

One of the primary aims of this paper is to generalize the kurt-spectra used in [17, 18] in the presence of a realistic *Euclid*-type mask and noise. Using a suite of state-of-the-art numerical simulations, we study the gravity-induced non-Gaussianity using weak lensing convergence κ maps. The gravity-induced signal is sufficient to saturate the Fisher bounds

[8]Many studies have also focused on one-point statistics for probing higher-order statistics. These include the well-known real-space one-point statistics such as the cumulants [47] or two-point cumulant correlators as well as the associated probability distribution function [48], the peak-count statistics [49], and morphological estimators [50].

JCAP11(2022)020

for all-sky low-noise maps expected from *Euclid*. Note that this might not be the case for ongoing surveys that are noise dominated and cover a small fraction of the sky; for these studies, an optimization in line with what was presented in [17, 18] may be necessary. Such procedures are, however, only optimal in the limit of weak non-Gaussianity, and may not be relevant for signal-dominated data from future surveys. We will thus simply stick to sub-optimal estimators in this work, and further neglect PNG though it can be incorporated the same framework. Generalizations of our estimators to spectroscopic galaxy redshift surveys such as BOSS[9] [51] or WiggleZ[10] [52] that probe the mass distribution of galaxies as biased tracers [53] are left for future work.

This paper is organized as follows. In section 2, we review the formalism for computing angular trispectra and describe the analytical modeling of gravity-induced trispectra that we adopt in this work. In section 3, we describe the trispectrum of weak lensing convergence and introduce the kurt-spectra. The ray-tracing simulations that we have used and the results obtained are presented in section 4. We conclude and discuss future prospects in section 5.

2 Formalism

We begin with a short review of n-point correlation functions in harmonic space in section 2.1, focusing on the case $n = 4$. We describe the computational methods for the angular trispectrum in section 2.2 and the theoretical models for the matter trispectrum used in our analysis in section 2.3.

2.1 Correlators in harmonic space

In cosmological observations, a projected observable $\mathcal{O}$ located at some redshift z is measured as a function of its angular position on the celestial sphere. This is usually thought as tracing the underlying matter density contrast δ integrated along the line-of-sight direction $\hat{n}$, weighted by some kernel $W_{\mathcal{O}}$ as

$$\mathcal{O}(z,\hat{n}) = \int_0^{\chi(z)} d\chi' \, W_{\mathcal{O}}(\chi')\delta(\chi',\chi'\hat{n}) \,, \tag{2.1}$$

where χ is the comoving radial distance. It is often useful to take advantage of the spatial isotropy of the celestial sphere and work in harmonic space, which allows for a spectral analysis. Expanding the real-space observable in spherical harmonics as $\mathcal{O}(z,\hat{n}) = \sum_{\ell=0}^{\infty}\sum_{m=-\ell}^{\ell}\mathcal{O}^{(z)}_{\ell m}Y_{\ell m}(\hat{n})$, the harmonic coefficients are obtained through the projection integral

$$\mathcal{O}^{(z)}_{\ell m} = 4\pi i^{\ell}\int_0^{\chi(z)} d\chi' \, W_{\mathcal{O}}(\chi')\int \frac{d^3k}{(2\pi)^3}\, j_{\ell}(k\chi')Y^*_{\ell m}(\hat{k})\delta(\chi',\boldsymbol{k}) \,, \tag{2.2}$$

where we have Fourier transformed δ and projected the plane waves onto the spherical harmonics basis. The n-point function in harmonic space is then obtained by taking the expectation value of a product of harmonic coefficients as

$$\langle \mathcal{O}^{(z_1)}_{\ell_1 m_1}\cdots\mathcal{O}^{(z_n)}_{\ell_n m_n}\rangle = (4\pi)^n i^{\ell_{1\cdots n}}\int\prod_{i=1}^{n}\left[\frac{d\chi_i' d^3k_i}{(2\pi)^3}W_{\mathcal{O}_i}(\chi_i')j_{\ell_i}(k_i\chi_i')Y^*_{\ell_i m_i}(\hat{k}_i)\right]\langle\delta_1\cdots\delta_n\rangle \,, \tag{2.3}$$

[9] http://www.sdss3.org/surveys/boss.php.
[10] http://wigglez.swin.edu.au/.

JCAP11(2022)020

where we defined $\ell_{1\cdots n} \equiv \ell_1 + \cdots + \ell_n$, $\mathcal{O}_i \equiv \mathcal{O}^{(z_i)}_{\ell_i m_i}$, and $\delta_i \equiv \delta(z_i, \boldsymbol{k}_i)$. In general, it is a challenging task to evaluate the convoluted multi-dimensional projection integrals appearing in (2.3) for $n \geq 3$. However, as we will shortly review, these integrals become factorized for δ-correlation functions that respect a certain separability condition, rendering the computation of higher-point functions much more feasible.

Our primary interest in this work will be the case $n = 4$, namely the angular trispectrum in harmonic space. A nice feature of a harmonic-space analysis is that we can completely factor out the azimuthal dependence and write the harmonic-space trispectrum as [13, 54]

$$\begin{aligned}\langle \mathcal{O}^{(z_1)}_{\ell_1 m_1} \cdots \mathcal{O}^{(z_4)}_{\ell_4 m_4} \rangle &= \sum_{LM} (-1)^M \begin{pmatrix} \ell_1 & \ell_2 & L \\ m_1 & m_2 & M \end{pmatrix} \begin{pmatrix} \ell_3 & \ell_4 & L \\ m_3 & m_4 & -M \end{pmatrix} T^{\ell_1\ell_2}_{\ell_3\ell_4}(L) \\ &= \sum_{LM} (-1)^M \begin{pmatrix} \ell_1 & \ell_2 & L \\ m_1 & m_2 & M \end{pmatrix} \begin{pmatrix} \ell_3 & \ell_4 & L \\ m_3 & m_4 & -M \end{pmatrix} P^{\ell_1\ell_2}_{\ell_3\ell_4}(L) + (2 \leftrightarrow 3) + (2 \leftrightarrow 4)\,,\end{aligned} \tag{2.4}$$

where $\sum_{LM} \equiv \sum_{L=0}^{\infty} \sum_{m=-L}^{L}$ and the rounded-bracketed matrices represent the Wigner 3-j symbols. In the second line, we have split the trispectrum into three different pairings of multipoles using permutation symmetry. As can be seen from (2.3), the input for the angular trispectrum is the matter trispectrum in Fourier space, which we can write as

$$\langle \delta_1 \cdots \delta_4 \rangle = T_\delta(\{z_i, \boldsymbol{k}_i\}) \times (2\pi)^3 \delta_D(\boldsymbol{k}_1 + \cdots + \boldsymbol{k}_4)\,, \tag{2.5}$$

where $\{z_i, \boldsymbol{k}_i\} = \{z_1, k_1, \cdots, z_4, k_4\}$ denotes the set of arguments and δ_D represents the Dirac delta function that ensures spatial translational invariance. In accordance with (2.4), the trispectrum can be decomposed into three different channels as

$$T_\delta(\{z_i, \boldsymbol{k}_i\}) = T^{(s)}_\delta(\{z_i, \boldsymbol{k}_i\}) + T^{(t)}_\delta(\{z_i, \boldsymbol{k}_i\}) + T^{(u)}_\delta(\{z_i, \boldsymbol{k}_i\})\,, \tag{2.6}$$

where we defined $s = |\boldsymbol{k}_1 + \boldsymbol{k}_2|$, $t = |\boldsymbol{k}_1 + \boldsymbol{k}_4|$, $u = |\boldsymbol{k}_1 + \boldsymbol{k}_3|$, and different channels are related by the permutations $2 \leftrightarrow 3$ and $2 \leftrightarrow 4$. These s, t, u-channel contributions are thus in one-to-one correspondence with $P^{\ell_1\ell_2}_{\ell_3\ell_4}(L)$, $P^{\ell_1\ell_4}_{\ell_3\ell_2}(L)$, $P^{\ell_1\ell_3}_{\ell_2\ell_4}(L)$, respectively, in (2.4).

Note that the (reduced) angular trispectrum $T^{\ell_1\ell_2}_{\ell_3\ell_4}(L)$ in (2.4) is defined with respect to a particular pairing of multipoles that corresponds to the s-channel. Unlike in Fourier space, different multipole pairings in harmonic space do not contribute to the total trispectrum in a simple additive manner, but instead they are related by [13]

$$\begin{aligned}T^{\ell_1\ell_2}_{\ell_3\ell_4}(L) &= P^{\ell_1\ell_2}_{\ell_3\ell_4}(L) \\ &+ (2L+1) \sum_{L'} \left((-1)^{\ell_2+\ell_3} \begin{Bmatrix} \ell_1 & \ell_2 & L \\ \ell_4 & \ell_3 & L' \end{Bmatrix} P^{\ell_1\ell_3}_{\ell_2\ell_4}(L') + (-1)^{L+L'} \begin{Bmatrix} \ell_1 & \ell_2 & L \\ \ell_3 & \ell_4 & L' \end{Bmatrix} P^{\ell_1\ell_4}_{\ell_3\ell_2}(L') \right),\end{aligned} \tag{2.7}$$

where the curly-bracketed matrices represent the Wigner 6-j symbols. Despite there being a complicated relation amongst three channels, it turns out that a simplifying approximation $T^{\ell_1\ell_2}_{\ell_3\ell_4}(L) \approx P^{\ell_1\ell_2}_{\ell_3\ell_4}(L)$ is often adequate for most purposes (see e.g. [13, 23]). This dramatically simplifies numerical analyses of harmonic-space trispectra; we adopt this approximation in this work.

As was alluded to above, the projection integrals in (2.3) become dramatically simplified for δ-correlation functions that are *separable*. Roughly speaking, a separable correlation function means that its individual terms can be expressed as a product of some functions

JCAP11(2022)020

of momentum variables. The precise separability condition for the matter trispectrum put forward in [28] is that individual terms, say, in the s-channel can be expressed as

$$T_\delta^{(s)}(\{z_i, \boldsymbol{k}_i\}) \supset f_1(z_1, k_1) \cdots f_4(z_4, k_4) f_s(s) t^{2J}\,, \tag{2.8}$$

where J is a non-negative integer for local interactions.[11] The gravitationally-induced matter trispectrum that is relevant for our purpose has $J = 0$. In this case, the angular and radial integrals in (2.3) become completely factorized, with the separable term (2.8) in Fourier space resulting in the following form in harmonic space [28]:

$$P^{\ell_1\ell_2}_{\ell_3\ell_4}(L) = \frac{g^{\ell_1\ell_2 L} g^{\ell_3\ell_4 L}}{(2\pi^2)^5} \int_0^\infty dr\, r^2 I^{(1)}_{\ell_1}(r) I^{(2)}_{\ell_2}(r) \int_0^\infty dr'\, r'^2 I^{(3)}_{\ell_3}(r') I^{(4)}_{\ell_4}(r') J^{(s)}_L(r, r')\,, \tag{2.9}$$

where

$$g^{\ell_1\ell_2\ell_3} = \sqrt{\frac{(2\ell_1+1)(2\ell_2+1)(2\ell_3+1)}{4\pi}} \begin{pmatrix} \ell_1 & \ell_2 & \ell_3 \\ 0 & 0 & 0 \end{pmatrix} \tag{2.10}$$

is a geometric factor and

$$I^{(i)}_\ell(r) = 4\pi \int_0^{\chi(z)} d\chi'\, W_{\mathcal{O}}(\chi') \int_0^\infty dk\, k^2 f_i(z(\chi'), k) j_\ell(k\chi') j_\ell(kr)\,, \tag{2.11}$$

$$J^{(s)}_L(r, r') = 4\pi \int_0^\infty ds\, s^2 f_s(s) j_L(sr) j_L(sr')\,, \tag{2.12}$$

are the projection radial integrals, with j_ℓ the spherical Bessel function. Typically, the functions of momenta take the form $f_i(z, k) = D_+^{m_i}(z) k^{2n_i} P_\delta^{p_i}(k)$, where D_+ is the linear growth function, P_δ is the matter power spectrum, and n_i, m_i, p_i are integers.[12] This allows us to further simplify the double integral in (2.11), as we show next.

A few comments about eq. (2.7) and the subsequent approximation are in order. The evaluation of the expression given in eq. (2.7) for the trispectrum is computationally challenging. This approximation was introduced in the context of CMB studies. In the case of low-redshift weak lensing studies, the situation is even more difficult due to the line-of-sight integration.

An alternative to this approach was introduced in [58] (also see [59]), where the spherical sky expression is replaced by the corresponding flat-sky approximations, and the 3j- and 6j-symbols are replaced by Dirac delta functions. The summations that appear in all-sky calculations are subsequently replaced by integrals that can be carried out using higher-dimensional Monte Carlo computations.

The primary aim of this article is to introduce the kurt-spectra and their higher-order analogs. A more accurate modeling will be taken up in the future. This is likely to take a hybrid approach, where the entire range of ℓ values is split into a low-ℓ and a high-ℓ regime. The low-ℓ ($\ell < 100$) regime can be tackled using an all-sky calculation, where 6j-symbols computations are feasible, and a flat-sky method will be used for the high-ℓ regime.

[11] See e.g. [22, 55] for alternative separability criteria for trispectra.

[12] More generally, one needs to introduce a scale-dependence in the linear growth function due to e.g. massive neutrinos. Such cases can be efficiently dealt with by the use of a polynomial approximation that separates the scale and redshift dependences; see [56, 57] for details.

JCAP11(2022)020

2.2 Computational methods

As we just saw, the computation of harmonic-space trispectra amounts to evaluating the projection integrals of the form (2.11) and (2.12). Naively, the presence of highly oscillatory Bessel functions in the integrand makes a direct numerical integration quite difficult, especially for high multipoles. Over recent years, efficient semi-analytic methods for evaluating these projection integrals have been developed in [28, 60–62] based on the algorithm known as the FFTLog [63], with the goal of computing angular observables in cosmology in a numerically fast and accurate way (see [57, 64–73] for related developments and applications of these methods).

The basic idea of these methods is to discrete Fourier transform (in $\log k$) the matter power spectrum over some finite interval $[k_{\rm min}, k_{\rm max}]$ as

$$P_\delta(z,k) \approx \sum_{m=-N/2}^{N/2} c_m(z) k^{-b+i\eta_m}\,, \quad \eta_m \equiv \frac{2\pi m}{\log(k_{\rm max},k_{\rm min})}\,, \tag{2.13}$$

where b is a real parameter introduced for convenience and the coefficients of the transform are given by

$$c_m(z) = \frac{2-\delta_{|m|,N/2}}{2N} \sum_{n=0}^{N-1} P_\delta(z,k_n) k_n^b k_{\rm min}^{-i\eta_m} e^{-2\pi i m n/N}\,. \tag{2.14}$$

Essentially, the FFTLog approximates the matter power spectrum in terms of a finite number of complex power-law functions, with a sub-percent accuracy for $N = O(10^2)$. The usefulness of this approximation is that the momentum integrals in (2.11) and (2.12) can now be done analytically for each complex power-law function, allowing us to express them as

$$I_\ell^{(i)}(r) \approx \sum_m c_m \int_0^{\chi(z)} d\chi'\, \chi'^{-\nu_m} D_+^{m_i}(z(\chi')) W_{\mathcal{O}}(\chi') \mathsf{I}_\ell\left(\nu_m, \frac{\chi'}{r}\right)\,, \tag{2.15}$$

$$J_L(r,r') \approx \sum_m c_m r^{-\nu_m} \mathsf{I}_L\left(\nu_n, \frac{r'}{r}\right)\,, \tag{2.16}$$

with [60]

$$\begin{aligned}\mathsf{I}_\ell(\nu,w) &\equiv 4\pi \int_0^\infty dx\, x^{\nu-1} j_\ell(x) j_\ell(wx) \\ &= \frac{2^{\nu-1}\pi^2 \Gamma(\ell+\frac{\nu}{2})}{\Gamma(\frac{3-\nu}{2})\Gamma(\ell+\frac{3}{2})} w^\ell\, {}_2F_1\left(\frac{\nu-1}{2}, \ell+\frac{\nu}{2}, \ell+\frac{3}{2}, w^2\right)\,,\end{aligned} \tag{2.17}$$

for $w \leq 1$, and ${}_2F_1$ denotes the Gauss hypergeometric function. For $w > 1$, one uses the property $\mathsf{I}_\ell(\nu,w) = w^{-\nu}\mathsf{I}_\ell(\nu,\frac{1}{w})$. Since the hypergeometric function is a smooth function whose analytic properties are well known, this provides an efficient way to compute the projection integrals, avoiding the need to directly integrate the Bessel functions.

If we restrict to large multipoles and sufficiently smooth line-of-sight kernels, then there is a more widely used approximation to deal with the projection integrals known as the Limber approximation [74, 75]. This amounts to replacing the spherical Bessel functions j_ℓ

JCAP11(2022)020

in the integrands with Dirac delta functions, $j_\ell(x) \approx \sqrt{\frac{\pi}{2\ell}}\delta_D(\ell - x)$, which leads to

$$I_\ell^{(i)}(r) \approx \frac{2\pi^2}{r^2} D_+^{m_i}(r) W_{\mathcal{O}}(r) \tilde{f}_i(\ell/r)\,, \tag{2.18}$$

$$J_L^{(s)}(r, r') \approx \frac{2\pi^2}{r^2} f_s(L/r)\delta_D(r - r')\,, \tag{2.19}$$

where $\tilde{f}_i$ is f_i evaluated at $z = 0$. Note that what used to be the χ integrand does not carry any multipole dependence, allowing us to factor it out from individual terms. Moreover, the leftover delta function in $J_L^{(s)}$ removes one of the radial integrals in (2.9). As a consequence, the Limber-approximated angular trispectrum simply reduces to the following one-dimensional integral (at tree level):

$$P^{\ell_1\ell_2}_{\ell_3\ell_4}(L) \approx g^{\ell_1\ell_2 L} g^{\ell_1\ell_2 L} \int_0^\infty \frac{dr}{r^6}\, D_+^6(r) W_{\mathcal{O}}^4(r) \tilde{T}_\delta^{(s)}\left(\frac{\ell_1}{r}, \cdots, \frac{\ell_4}{r}, \frac{L}{r}\right)\,, \tag{2.20}$$

where $\tilde{T}_\delta^{(s)}$ is defined to be the purely momentum-dependent part of the matter trispectrum

$$\tilde{T}_\delta^{(s)}(k_1, \cdots, k_4, s) = T_\delta^{(s)}(\{z_i, \boldsymbol{k}_i\})|_{z_i=0}\,, \tag{2.21}$$

with the normalization $D_+(0) = 1$. Similar expressions exist for the t- and u-channels. We will show a comparison of the FFTLog and Limber approximation in section 3.1.

2.3 Theoretical model for matter trispectrum

Cosmological angular trispectra are obtained by projecting the matter trispectrum along the line of sight. While this in principle involves integrating over all momenta, typical scales are related by $\ell \sim k\chi(z)$ between the harmonic and Fourier domains. Depending on the harmonics, two distinct theoretical models for matter clustering are then relevant in the quasi-linear and nonlinear regimes. Let us briefly review the models that we consider in our study.

Quasi-linear regime. At sufficiently large scales, cold dark matter behaves as an effective pressureless fluid, and its gravitational evolution is governed by the Newtonian fluid equations of motion. In the standard perturbation theory (SPT) framework [76], these equations are solved perturbatively by expanding the nonlinear density contrast in terms of the linear solution $\delta^{(1)}$ as

$$\delta(z, \boldsymbol{k}) = \sum_{n=1}^{\infty} D_+^n(z) \int_{\boldsymbol{q}_1, \cdots, \boldsymbol{q}_n} (2\pi)^3 \delta_D(\boldsymbol{k} - \boldsymbol{q}_{1\cdots n}) F_n^{\rm sym}(\boldsymbol{q}_1, \cdots, \boldsymbol{q}_n) \delta^{(1)}(\boldsymbol{q}_1) \cdots \delta^{(1)}(\boldsymbol{q}_n)\,, \tag{2.22}$$

where $\int_{\boldsymbol{q}_1, \cdots, \boldsymbol{q}_n} \equiv \int \prod_{i=1}^n \frac{d^3 q_i}{(2\pi)^3}$, $q_{1\cdots n} \equiv \boldsymbol{q}_1 + \cdots \boldsymbol{q}_n$ and $F_n^{\rm sym}$ is the symmetrized SPT kernel [77, 78]. The Einstein-de Sitter (matter domination) approximation is typically used so that the temporal and spatial dependences become factorized in the way above. At tree level, there are two contributions to the matter trispectrum

$$T_\delta^{\rm SPT}(\{z_i, \boldsymbol{k}_i\}) = T_{3111}(\{z_i, \boldsymbol{k}_i\}) + T_{2211}(\{z_i, \boldsymbol{k}_i\})\,, \tag{2.23}$$

which follows from the two distinct ways of expanding δ. We quote here the standard results from the SPT [76]

$$T_{3111}(\{z_i, \boldsymbol{k}_i\}) = 6 D_1 D_2 D_3 D_4^3 P_1 P_2 P_3 F_3^{\rm sym}(\boldsymbol{k}_1, \boldsymbol{k}_2, \boldsymbol{k}_3) + 3 \text{ perms}\,, \tag{2.24}$$

$$T_{2211}(\{z_i, \boldsymbol{k}_i\}) = 4 D_1 D_2^2 D_3 D_4^2 P_1 P_3 P_s F_2^{\rm sym}(\boldsymbol{k}_1, -\boldsymbol{k}_{12}) F_2^{\rm sym}(\boldsymbol{k}_3, \boldsymbol{k}_{12}) + 11 \text{ perms}\,, \tag{2.25}$$

JCAP11(2022)020

where we used the notation $D_i \equiv D_+(z_i)$ and $P_i \equiv P_\delta^{\rm L}(k_i)$ for the linear matter power spectrum. To utilize the separability, we express the above trispectrum in terms of momentum magnitudes and write the total tree-level trispectrum as

$$T_\delta^{\rm SPT}(\{z_i, \boldsymbol{k}_i\}) = \left[T^{(s)}_{\rm exchange}(k_1, k_2, k_3, k_4, s) + 2 \text{ perms}\right] + T_{\rm contact}(k_1, k_2, k_3, k_4)\,, \tag{2.26}$$

where the labels "exchange" and "contact" refer to the parts that depend on the internal momenta and that does not, respectively. Explicit expressions of the matter trispectrum in these variables can be found in [28].

Nonlinear regime. In the nonlinear regime $\delta \gtrsim 1$, the perturbation theory breaks down and we typically have to resort to phenomenological models or fitting functions. Unlike for the bispectrum, there currently exists no precise fitting function available for the matter trispectrum that smoothly interpolates between linear and nonlinear scales for all momentum configurations.[13] Instead, a nonlinear clustering model known as the *hierarchical ansatz* (HA) [81] is often invoked.

In the HA, higher-order spectra of density contrast are written as a sum of product of two-point functions over all possible topologies with different amplitudes. The matter trispectrum then has two contributions given by [82, 83]

$$\begin{aligned} T_\delta^{\rm HA}(\boldsymbol{k}_1, \cdots, \boldsymbol{k}_4) \equiv\, & R_a([P_\delta^{\rm NL}(k_1)]^{1+\epsilon}[P_\delta^{\rm NL}(k_2)]^{1+\epsilon}[P_\delta^{\rm NL}(k_3)]^{1+\epsilon} + 3 \text{ perms}) \\ & + R_b([P_\delta^{\rm NL}(k_1)]^{1+\epsilon}[P_\delta^{\rm NL}(k_3)]^{1+\epsilon}[P_\delta^{\rm NL}(s)]^{1+\epsilon} + 11 \text{ perms})\,, \end{aligned} \tag{2.27}$$

where $P_\delta^{\rm NL}$ denotes the nonlinear matter power spectrum and we have suppressed the redshift dependence. We will only consider the models with $\epsilon = 0$ in this paper. The matter trispectrum in the HA is therefore parameterized by two amplitudes R_a and R_b, which are assumed to be constant in the strongly nonlinear regime. Note that each of the two structures in the HA trispectrum has the same power spectra dependence as T_{3111} and T_{2211} in the tree-level trispectrum, and the amplitudes R_a, R_b can be thought as being the angular averages of the SPT kernels [76, 84, 85], e.g. $R_a = \langle F_3\rangle_\Omega$, $R_b = \langle F_2\rangle_\Omega^2$, where $\langle F_n\rangle_\Omega \equiv n! \int [\prod_{i=1}^n \frac{d\Omega_i}{4\pi}] F_n(\boldsymbol{k}_1, \cdots, \boldsymbol{k}_n)$. Sometimes a simpler model is used for which the two amplitude parameters in (2.27) are set equal, $R_a = R_b = Q_4$. It was checked, for instance, in [86] that this choice fits the simulation results well in the nonlinear regime for certain kinematic configurations. For our comparison against simulations, we have taken Q_4 as a free parameter to fit the data.

The HA trispectrum has a very different momentum dependence from that of the SPT trispectrum, so that it is only applicable in the strongly nonlinear regime. This is manifest from the soft limit behavior of the two shapes: $T_\delta^{\rm HA} \sim P_\delta(k_1)$ as $k_1 \to 0$, while $T_\delta^{\rm SPT} \sim \frac{1}{k_1} P_\delta(k_1)$ in the same limit. In the next section, we compare the shapes of the weak lensing trispectrum arising from these two models.

There are many different HA available in the literature. The specific version that we have used was introduced in [87, 88]. In this model the amplitudes associated with diagrams with different topologies but with same number of vertices are always equal. This is not only

[13] The second-order SPT kernel F_2 that characterizes the matter bispectrum has 3 independent tensor structures. A fitting formula is then constructed by endowing each of these structures with a general function momenta that interpolates the linear and nonlinear regimes, see e.g. [79]. On the other hand, the matter trispectrum depends on the third-order kernel F_3 that has 12 independent tensor structures with 6 momentum degrees of freedom, which complicates such a fitting procedure (see [80] for recent progress on this).

JCAP11(2022)020

assumed at the level of fourth-order (trispectrum) but to an arbitrary order. Other models that are well known include the minimal hierarchical model which was introduced by [89]. In [90, 91] many consequences of minimal hierarchical models for weak lensing were discussed. Many other versions of HA were tested subsequently. One such model assumes $R_b \neq 0$ and $R_a = 0$ [47, 92]. In general, it was found that various choices of R_a and R_b can reproduce the weak lensing statistics with varying success. There is no specific HA that can reproduce all observables. Moreover, most previous studies concentrate on one-point statistics. In a related context we have also checked that the kurtosis spectra extracted from a simulated log-normal sky is very different from the more realistic ray-traced simulations. This is important as log-normal simulations are routinely used in field-based inference studies. We have also tried the extension of the log-normal [93] model, but they could not be fine-tuned to reproduce the both kurtosis spectra for the entire range of redshift and angular harmonics probed. A full modeling of matter trispectrum would involve either (a) effective halo model type approach for trispectrum that extends to higher order [94] or (b) a fitting function for the trispectrum as was done most recently by [95] for the bipectrum. For individual shapes of trispectrum [96], we use estimators developed in [97] for the study of shapes of bispectrum.

3 Weak lensing higher-order statistics

In this section we compute the weak lensing trispectrum and introduce the kurt-spectra. The weak lensing convergence κ is a line-of-sight integration of the underlying density contrast δ, and can be expressed using the lensing kernel W_κ as

$$\kappa(\hat{n}) = \int_0^{\chi_s} d\chi' \, W_\kappa(\chi') \delta(\chi', \chi'\hat{n}) \,, \tag{3.1}$$

$$W_\kappa(\chi) = \frac{3H_0^2\Omega_m(1+z(\chi))}{2c^2} \int_\chi^{\chi_s} d\chi' n(\chi') \frac{\chi'-\chi}{\chi'} \,, \tag{3.2}$$

where $n(\chi)$ represents the distribution of lensing sources. In our study, we will assume all sources to be at a single source plane $\chi = \chi_s$, which gives $W_\kappa(\chi) = 3H_0^2\Omega_m(1+z(\chi))\chi(\chi_s - \chi)\Theta(\chi_s - \chi)/(2c^2\chi_s)$. The spherical harmonic coefficients $\kappa_{\ell m}$ of the convergence κ map is defined through $\kappa_{\ell m} \equiv \int d\hat{n}\, \kappa(\hat{n}) Y^*_{\ell m}(\hat{n})$.

3.1 Weak lensing trispectrum

Using the formalism described in the previous section, we can straightforwardly compute the trispectrum of weak lensing convergence in harmonic space. Figure 1 shows the shape of the weak lensing trispectrum for various multipole configurations. We show the reduced part of the trispectrum $\tau^{\ell_1\ell_2}_{\ell_3\ell_4}(L)$ after stripping off the geometric factors, defined by

$$P^{\ell_1\ell_2}_{\ell_3\ell_4}(L) = g^{\ell_1\ell_2 L} g^{\ell_3\ell_4 L} \tau^{\ell_1\ell_2}_{\ell_3\ell_4}(L) \,, \tag{3.3}$$

at source redshift $z_s = 1$. We considered the weak lensing trispectrum arising from two different theoretical models for the matter trispectrum: the tree-level result from the SPT (blue curves) and the HA (black curves) with $R_a = R_b = 1$. As the figure shows, these two models lead to drastically different scaling behaviors, clearly highlighting the different domains of applicability of these models. In particular, the HA leads to a less suppressed power compared to the tree-level signal at small scales, as expected for a nonlinear clustering model.

JCAP11(2022)020

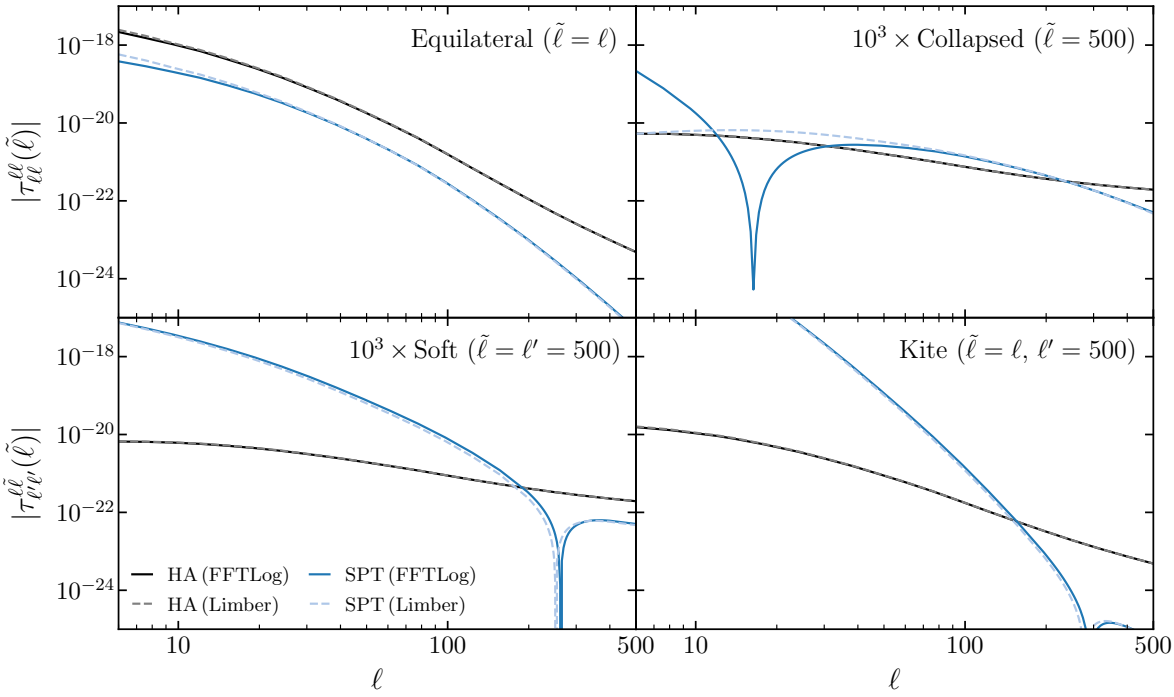

Figure 1. Weak lensing trispectrum at $z_s = 1$ after stripping off the geometric factors, cf. (3.3). Two different models for the matter trispectrum are used: the tree-level result from the standard perturbation theory (SPT) and the hierarchical ansatz (HA) with $R_a = R_b = 1$. The solid and dashed lines show the trispectra computed using the FFTLog and the Limber approximation, respectively.

It is interesting to compare the calculations done with the FFTLog and the Limber approximation.[14] We see that the Limber approximation in general works very well for weak lensing even for very small multipoles, but there is a notable exception: the SPT trispectrum in the collapsed limit $L \ll \ell_1, \cdots, \ell_4$, for which the Limber approximation induces a large deviation. This can be understood from the way the matter trispectrum in Fourier space is projected to harmonic space: the collapsed limit is dominated by terms that scale as inverse powers of s in the SPT trispectrum. It turns out that these terms fully cancel in the rhombus-like configurations $k_1 = k_2 = k_3 = k_4$ in Fourier space, ensuring the infrared safety of the one-loop power spectrum and that the consistency relations are satisfied [98]. While this continues to be true under the Limber approximation that simply amounts to the substitution $k_i \to \frac{\ell_i}{r}$ (cf. (2.20)), these terms do not fully cancel in the exact calculation when the projection is taken before taking the equal-multipole limit. The FFTLog method is able to capture this non-cancellation of terms that dominate in the collapsed limit, hence resulting in the large difference between the two computational methods in the collapsed limit. This implies that the Limber approximation of the weak lensing trispectrum from the SPT is highly accurate for most configurations, except in the limit $L \to 0$.[15] For the HA, the Limber approximation was found to be accurate for the multipole configurations we considered.

[14] In figure 1, we used the FFTLog only for the external multipoles and used the Limber approximation for the internal L to reduce computational costs.

[15] The same observation was made in [28], where it was shown that the Limber approximation fails for the computation of the non-Gaussian covariance of the angular matter power spectrum, which requires evaluating $T^{\ell_1\ell_2}_{\ell_3\ell_4}(L)$ at $L = 0$.

JCAP11(2022)020

3.2 Kurt-spectra

While the precise physical content of a correlation function is contained in its entire shape dependence, it is often useful to construct lower-point statistics to estimate higher-point functions. One of the main advantages of such estimators is that they have a much simpler multipole dependence, while still carrying sufficient information to constrain amplitude-like parameters.

The harmonic coefficients of the n-th power of the convergence field, κ^n, can be expressed in terms of $\kappa_{\ell m}$ as

$$\begin{aligned}[\kappa^n]_{\ell m} &\equiv \int d\hat{\Omega}\, \kappa^n(\hat{\Omega}) Y^*_{\ell m}(\hat{\Omega}) \\ &= \sum_{\ell_1 m_1} \cdots \sum_{\ell_n m_n} \kappa_{\ell_1 m_1} \cdots \kappa_{\ell_n m_n} \int d\hat{\Omega}\, Y_{\ell_1 m_1}(\hat{\Omega}) \cdots Y_{\ell_n m_n}(\hat{\Omega}) Y^*_{\ell m}(\hat{\Omega}). \end{aligned} \tag{3.4}$$

The integral involving spherical harmonics above can be expressed in terms of (products and sums of) the Wigner 3-j symbols. We can then define the following two *kurt-spectra*, which we will denote as K^{22}_ℓ and K^{31}_ℓ [17, 18]:

$$K^{22}_\ell \equiv \frac{1}{2\ell+1} \sum_m \langle [\kappa^2]_{\ell m} [\kappa^2]^*_{\ell m} \rangle = \sum_{\ell_1 \cdots \ell_4} \frac{g^{\ell_1 \ell_2 \ell} g^{\ell_3 \ell_4 \ell}}{(2\ell+1)^2} T^{\ell_1 \ell_2}_{\ell_3 \ell_4}(\ell)\,, \tag{3.5}$$

$$K^{31}_\ell \equiv \frac{1}{2\ell+1} \sum_m \Re \langle [\kappa^3]_{\ell m} \kappa^*_{\ell m} \rangle = \sum_{\ell_1 \ell_2 \ell_3 L} \frac{g^{\ell_1 \ell_2 L} g^{\ell_3 \ell L}}{(2L+1)(2\ell+1)} T^{\ell_1 \ell_2}_{\ell_3 \ell}(L)\,, \tag{3.6}$$

where we have expressed the results in terms of the weak lensing angular trispectrum $T^{\ell_1 \ell_2}_{\ell_3 \ell_4}(L)$ and $\Re$ denotes the real part.[16] These are natural generalizations of the skew-spectrum $\langle [\kappa^2]_{\ell m} \kappa^*_{\ell m} \rangle$ statistics studied in [99] to fourth order.[17]

The Gaussian (disconnected) contribution to the trispectrum, which we denote by $G^{\ell_1 \ell_2}_{\ell_3 \ell_4}(L)$, depends only on the angular power spectrum $C_\ell = \langle \kappa_{\ell m} \kappa^*_{\ell m} \rangle$, and is given by the expression [13]

$$\begin{aligned} G^{\ell_1 \ell_2}_{\ell_3 \ell_4}(L) = (-1)^{\ell_1+\ell_3} &\sqrt{(2\ell_1+1)(2\ell_3+1)} C_{\ell_1} C_{\ell_3} \delta_{L0} \delta_{\ell_1 \ell_2} \delta_{\ell_3 \ell_4} \\ &+ (2L+1) C_{\ell_1} C_{\ell_2} \left[(-1)^{\ell_2+\ell_3+L} \delta_{\ell_1 \ell_3} \delta_{\ell_2 \ell_4} + \delta_{\ell_1 \ell_4} \delta_{\ell_2 \ell_3} \right], \end{aligned} \tag{3.8}$$

where $\delta_{\ell_a \ell_b}$ denotes the Kronecker delta. The corresponding Gaussian contribution to the kurt-spectra are given by

$$G^{22}_\ell = \sum_{\ell_1 \ell_2 \ell_3 \ell_4} \frac{g^{\ell_1 \ell_2 \ell} g^{\ell_3 \ell_4 \ell}}{(2\ell+1)^2} G^{\ell_3 \ell_4}_{\ell_1 \ell_2}(\ell)\,, \tag{3.9}$$

$$G^{31}_\ell = \sum_{\ell_1 \ell_2 \ell_3 L} \frac{g^{\ell_1 \ell_2 \ell} g^{\ell_3 L \ell}}{(2L+1)(2\ell+1)} G^{\ell_3 \ell}_{\ell_1 \ell_2}(L)\,. \tag{3.10}$$

[16] The relations between the kurt-spectra and the trispectrum can be derived by using the inversion formula for the angular trispectrum

$$T^{\ell_1 \ell_2}_{\ell_3 \ell_4}(L) = (2L+1) \sum_{M, m_i} \begin{pmatrix} \ell_1 & \ell_2 & L \\ m_1 & m_2 & M \end{pmatrix} \begin{pmatrix} \ell_3 & \ell_4 & L \\ m_3 & m_4 & -M \end{pmatrix} \langle \kappa_{\ell_1 m_1} \cdots \kappa_{\ell_4 m_4} \rangle\,. \tag{3.7}$$

[17] For the skew-spectra applied to galaxy statistics, see also [100–102].

JCAP11(2022)020

These need to be subtracted from the total kurt-spectra. Substituting the Gaussian trispectrum (3.8), we get

$$G^{22}_\ell = \frac{1}{4\pi}\sum_{\ell_1\ell_2}(2\ell_1+1)(2\ell_2+1)C_{\ell_1}C_{\ell_2}\left[\delta_{\ell 0}+2\begin{pmatrix}\ell_1 & \ell_2 & \ell\\ 0 & 0 & 0\end{pmatrix}^2\right], \tag{3.11}$$

$$G^{31}_\ell = 3C_\ell \times \frac{1}{4\pi}\sum_{\ell'}(2\ell'+1)C_{\ell'}\,. \tag{3.12}$$

These two spectra are related to the real-space kurtosis by

$$\frac{1}{4\pi}\int d\hat{n}\,\langle\kappa^4(\hat{n})\rangle = \frac{3}{4\pi}\sum_\ell(2\ell+1)G^{22}_\ell = \frac{3}{4\pi}\sum_\ell(2\ell+1)G^{31}_\ell = 3\sigma^4\,, \tag{3.13}$$

where $\sigma^2 \equiv \frac{1}{4\pi}\int d\hat{n}\,\langle\kappa^2(\hat{n})\rangle = \frac{1}{4\pi}\sum_\ell(2\ell+1)C_\ell$ is the angle-averaged variance. To include the contribution from the noise, C_ℓ in (3.8) should be replaced by $C_\ell + N_\ell$. For Gaussian noise, the noise power spectrum is independent of ℓ: $N_\ell = 4\pi\sigma^2/N_{\rm pix}$.

In addition to the kurt-spectra at fourth order, we have also computed the fifth-, sixth- and seventh-order spectra from numerical simulations. At each order, there are more than one spectrum; for example, there are two fifth-order spectra defined as follows[18]

$$\Re\langle[\kappa^4]_{\ell m}\kappa^*_{\ell' m'}\rangle = C^{41}_\ell\delta_{\ell\ell'}\delta_{mm'}\,, \quad \Re\langle[\kappa^3]_{\ell m}[\kappa^2]^*_{\ell' m'}\rangle = C^{32}_\ell\delta_{\ell\ell'}\delta_{mm'}\,. \tag{3.14}$$

The triplets of sixth-order spectra C^{51}_ℓ, C^{42}_ℓ, C^{33}_ℓ and seventh-order spectra C^{61}_ℓ, C^{52}_ℓ, C^{43}_ℓ are defined analogously. Note that, unlike even-order spectra, there is no Gaussian contribution at odd orders. The addition of noise, typically assumed to be Gaussian, increases the scatter at odd orders, while for even orders it affects the mean of the estimator through its contribution to the disconnected components.

4 Comparison with ray-tracing simulations

Having described the calculation of the matter trispectrum and the weak lensing kurt-spectra, we now compare these theoretical signals to simulations. We first describe the details of the N-body simulations used in section 4.1 and then discuss the results in section 4.2.

4.1 Simulation specifications

We use the publicly available all-sky weak lensing maps generated by [103][19] using a ray-tracing scheme through N-body simulations. The underlying N-body simulations follow the gravitational clustering of 2048^3 particles. Multiple lens planes were used to generate the lensing convergence κ and the corresponding shear γ maps. To generate the maps in these simulations, the source redshifts used were in the range $z_s \in [0.05, 5.30]$ at a redshift-interval of $\Delta z_s = 0.05$. In this study, we have used the maps with source-redshifts $z_s = 0.5$, 1, and 2, using the following fiducial cosmological parameters: the dimensionless Hubble parameter

[18] While the harmonic mode decomposition and a related power spectral analysis is ideal for a higher sky coverage, for ongoing surveys with a small fraction of sky coverage it is often easier to work in the real-space domain to avoid complications related to irregular mask or survey geometry. The higher-order correlation functions corresponding to these high-order spectra are obtained by the usual Legendre transform as $C^{pq}(\theta) = \frac{1}{4\pi}\sum_\ell C^{pq}_\ell(2\ell+1)P_\ell(\cos\theta)$.

[19] http://cosmo.phys.hirosaki-u.ac.jp/takahasi/allsky_raytracing/.

JCAP11(2022)020

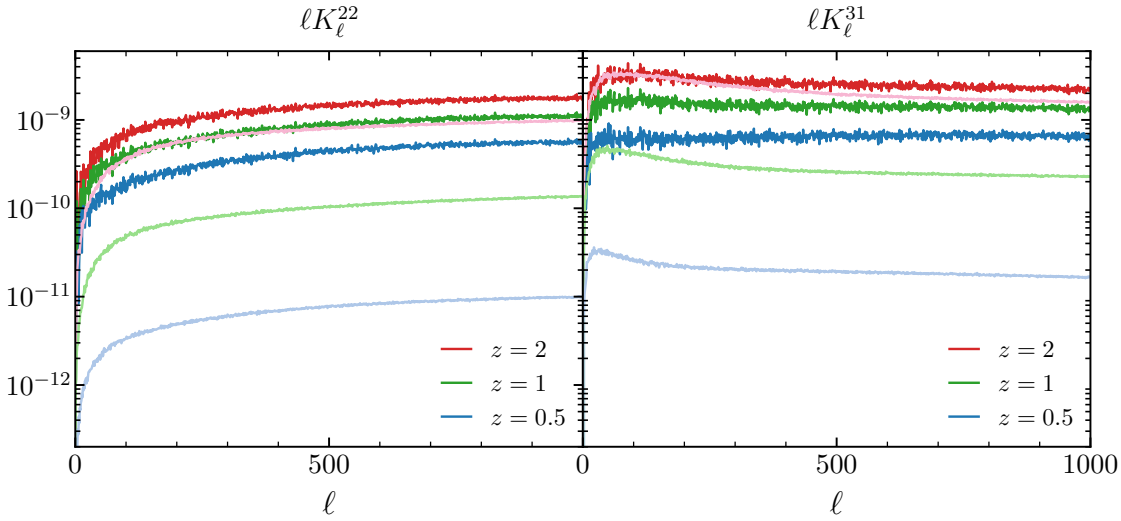

Figure 2. Kurt-spectra K_ℓ^{31} and K_ℓ^{22} as defined in (3.5) and (3.6), without any beam smoothing. In each panel, the (pale) red, green, and blue curves show the (Gaussian) kurt-spectra for source redshifts $z_s = 0.5$, 1, and 2, respectively. One single realization with $N_{\rm side} = 1024$ was used to generate the total kurt-spectra, while the Gaussian parts are generated using ten realizations of Gaussian maps from the theoretical power spectrum.

$h = 0.7$, the dark matter density $\Omega_{cdm} = 0.233$, the baryon density $\Omega_b = 0.046$, the matter density $\Omega_m = \Omega_{cdm} + \Omega_b$, the amplitude of matter fluctuations on $8h^{-1}$Mpc scales $\sigma_8 = 0.82$, the scalar spectral index $n_s = 0.97$, and a flat universe. In a previous study [104], inclusion of post-Born terms in lensing statistics were studied at the level of the bispectrum. Although post-Born corrections play a significant role at higher redshift, e.g. in the case of CMB lensing, it was found that such corrections play a negligible role at the low-source redshifts that we study in this work.

The lensing convergence maps were generated using an equal area pixelization scheme in `HEALPix`[20] format [105]. In this pixelization scheme, the number of pixels scales as $N_{\rm pix} = 12N_{\rm side}^2$. The resolution parameter $N_{\rm side}$ can take values $N_{\rm side} = 2^m$ with $m = 1, 2, \cdots$. The maps used in this study are generated at $N_{\rm side} = 4096$ and were cross-checked against higher-resolution maps constructed at $N_{\rm side} = 8192$, 16384 for consistency, up to $\ell_{\rm max} = 2 \times 10^3$. Many additional tests were also performed using the E/B decomposition of the shear maps for the construction of κ maps [103]. After this validation procedure, we have degraded these maps to $N_{\rm side} = 1024$ and analyzed them for harmonic modes satisfying $\ell \leq 2N_{\rm side}$.

4.2 Results and discussion

4.2.1 Shapes of Kurt-spectra

In figure 2, we show the redshift dependence and the shapes of the two kurt-spectra defined in (3.5) and (3.6) from a single realization, without an observational mask or noise. The various lines, from bottom to top in each panels, present the results for source redshifts $z_s = 0.5$, 1, and 2, respectively. We see that the amplitude of K_ℓ^{31} is typically higher than that of K_ℓ^{22} at low ℓ. This is because a larger number of non-vanishing trispectrum configurations contribute to the former at a given $\ell \ll \ell_{\rm max}$.

[20] https://healpix.jpl.nasa.gov/.

JCAP11(2022)020

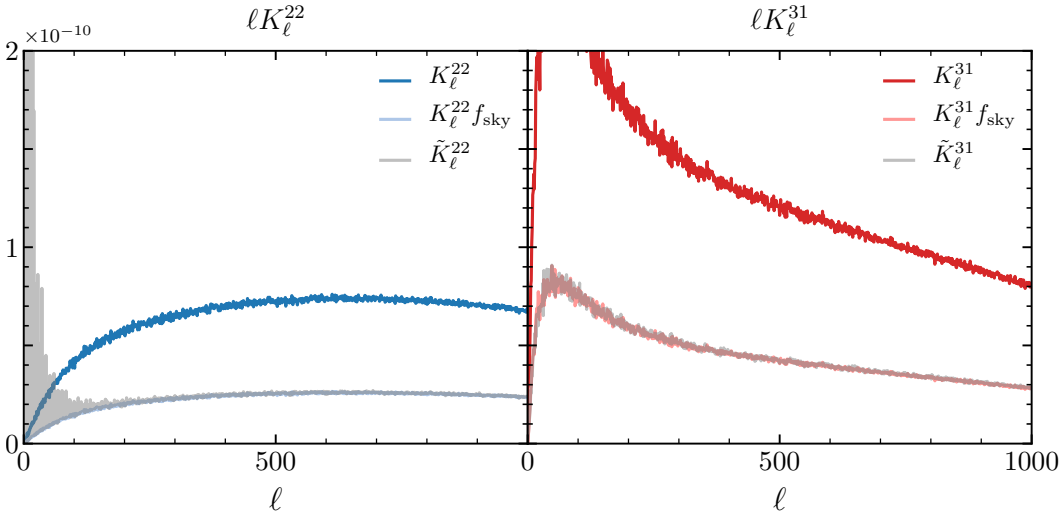

Figure 3. Kurt-spectra at $z_s = 1$ after applying a *Euclid*-type mask, with no noise inclusion. The smoothing angular scale is fixed at $\theta_s = 5'$. The upper curve shows K_ℓ^{pq} computed using a single realization without the observational mask. The two nearly-identical curves at the bottom show the corresponding masked spectra, $\tilde{K}_\ell^{pq}$, and the unmasked spectra multiplied with the fraction of sky coverage, $K_\ell^{pq} f_{\rm sky}$.

In addition to the total kurt-spectra, we have also generated ten Gaussian realizations to estimate the contribution to the kurt-spectra from the disconnected parts of the trispectrum, (3.10) and (3.9), which are shown in pale-colored lines. For generating these realizations, we have used the same power spectra as the original numerical simulations. As expected, the Gaussian contributions are subdominant at low redshifts where κ traces the highly non-Gaussian underlying density distribution. These simulated Gaussian kurt-spectra were found to match the theoretical signals accurately.

4.2.2 Observational mask and noise

Observational masks introduce mode couplings that need to be corrected before studying the gravity-induced mode coupling. An efficient approach was introduced in [106] to study the ordinary angular power spectrum, commonly known as the pseudo-C_ℓ or PCL technique. Using the PCL approach, an unbiased estimator for the $(p+q)-$th order power spectrum, $\hat{C}_\ell^{pq}$, can be expressed as

$$\hat{C}_\ell^{pq} = \sum_{\ell'} M_{\ell\ell'}^{-1} (\tilde{C}_{\ell'}^{pq} - \tilde{G}_{\ell'}^{pq}) \,, \tag{4.1}$$

where $\tilde{C}_\ell^{pq}$ represents the total spectrum estimated from a noisy map in the presence of mask

$$\tilde{C}_\ell^{pq} = \frac{1}{2\ell+1} \sum_m [\tilde{\kappa}^p]_{\ell m} [\tilde{\kappa}^q]_{\ell m} \,, \tag{4.2}$$

with $\tilde{\kappa}$ the masked κ map. The Gaussian component of the spectrum is denoted above as $\tilde{G}_\ell^{pq}$, which is computed using Monte Carlo realizations of Gaussian maps in the presence of the same mask and noise. The matrix $M_{\ell\ell'}$ that encodes the mode-coupling information induced by the mask takes the form

$$M_{\ell\ell'} = (2\ell'+1) \sum_{\ell''} \frac{2\ell''+1}{4\pi} |w_{\ell''}|^2 \begin{pmatrix} \ell & \ell' & \ell'' \\ 0 & 0 & 0 \end{pmatrix}^2 \,, \tag{4.3}$$

JCAP11(2022)020

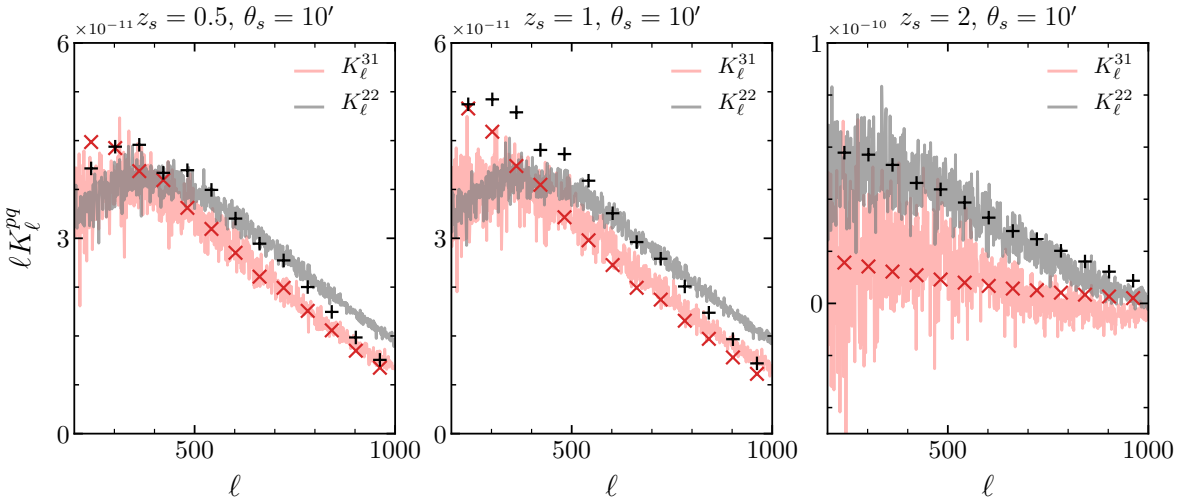

Figure 4. Comparison of theoretical and numerical results for the kurt-spectra with $\theta_s = 10'$. The discrete points represent theoretical predictions using the hierarchical ansatz. The simulation results are an average of ten realizations (see the text for more details).

where $w_{\ell\ell''}$ represents the angular power spectrum of the survey mask. In the high-ℓ regime, the coupling matrix simplifies as $M_{\ell\ell'} \approx f_{\rm sky}\delta_{\ell\ell'}$ with $f_{\rm sky}$ the fraction of sky coverage. For the spectra of order higher than four, terms involving lower-order spectra will contribute and generation of Gaussian maps may not be enough to subtract the disconnected contributions.

Using this technique, we study the effect of a *Euclid*-type mask in the estimation of the kurt-spectra. (For reference, the mask we have used has $f_{\rm sky} \approx 0.35$ and is described in [99].) The results are shown in figure 3, where the left and right panels show the kurt-spectra K_ℓ^{22} and K_ℓ^{31}, respectively. The smoothing angular scale is fixed at $\theta_s = 5'$ in both cases. In each panel, the upper curve shows K_ℓ^{pq} computed from a single realization without any noise added. The two nearly-identical curves at the bottom show the corresponding masked $\tilde{K}_\ell^{pq}$ and the rescaled unmasked spectra $f_{\rm sky}K_\ell^{pq}$. The same scaling with $f_{\rm sky}$ can be applied to the Gaussian contribution and the noise; hence these contributions can simply be subtracted to construct an unbiased estimator. We used a sharp mask without any apodization. The large-scale features of the mask then appear as fluctuations in the convolved spectra, which survive the auto-spectrum $\tilde{K}_\ell^{22}$ but not in the cross-spectrum $\tilde{K}_\ell^{31}$.

The estimator we have introduced here is a sub-optimal estimator.[21] This is sufficient for all-sky surveys where the signal-to-noise is very high. A nearly-optimal estimator which is also unbiased was considered for PNG in the CMB in [17, 18]. This method depends on applying weights that depend on the target trispectrum and is computationally more expensive. An optimal method was also presented in [17, 18], which involves inverse covariance weighting. Such estimators are optimal only in the limit of small non-Gaussianity (e.g. PNG). However, such an approach is neither realistic nor necessary for secondary non-Gaussianity where the non-Gaussian signal is quite strong. Optimized versions of the kurt-spectra have also been considered in [17] for PNG, though they cannot be estimated using a PCL estimator. In the presence of a mask, the linear correction terms require a more elaborate Monte Carlo computation involving Gaussian random realizations. Optimization of our estimator to the gravity-induced secondary non-Gaussianity will be presented elsewhere.

[21] The flat-sky equivalent of PCLs used here was developed in [107].

JCAP11(2022)020

4.2.3 Comparison with theory

In figures 4 and 5, we present the results of our comparison of a theoretical model against numerical simulations for source redshifts $z_s = 0.5$, 1, and 2. We have used two different smoothing angular scales $\theta_s = 10'$ and $\theta_s = 30'$, for which it was sufficient to use the maps with $N_{\rm side} = 512$ and $\ell_{\rm max} = 1024$. Two curves are shown in each panel: the red and gray curves represent K_ℓ^{31} and K_ℓ^{22}, respectively. For the purpose of comparing against purely theoretical signals from the connected trispectrum, we have subtracted the Gaussian contributions and no noise and mask were used. The discrete points represent the theoretical results using the HA given in (2.27) with $R_a = R_b$ as a free parameter to fit the data. As can be seen from the figures, the kurt-spectra resulting from the HA agree reasonably well with the simulation results in the nonlinear regime, while it has an upward trend and starts to display a large deviation towards low multipoles.[22]

We have also done a comparison with the tree-level SPT trispectrum used as the input, and found that they deviate significantly from the simulation results even at low ℓ, with or without using the Limber approximation. This failure can be attributed to the fact that the tree-level approximation typically remains valid up to the scale $k_\star \approx 0.1\,h\,{\rm Mpc}^{-1}$ in Fourier space, with the corresponding nonlinear multipoles $\ell_\star \approx 90$, 150, and 240 for $z_s = 0.5$, 1, and 2, respectively. The kurt-spectra therefore involve summing over a large number of nonlinear modes for the smoothing scales that we have considered in this work. For example, even the largest smoothing scale $\theta_s = 30'$ that we used only reduces the amplitude at $\ell_\star = 240$ by 30%, which is not sufficient to suppress the contribution from nonlinear modes.

The HA and SPT both generate similar correlation structure but with different hierarchical amplitudes R_a and R_b [76]. This explains the fact that in figure 4 the theoretical predictions better match numerical simulations for source redshift $z_s = 0.5$ (highly nonlinear regime) and $z_s = 2.0$ (quasi-linear regime). However, in the intermediate regime, the form of the correlation hierarchy is more complicated and remains poorly understood. This is reflected in the middle panel of figure 4 for $z_s = 1.0$. Indeed, the line-of-sight integral mixes various modes.

There are clear deviations in the high-ℓ regime especially for $z_s = 2.0$. The HA can be extended to consider $\epsilon \neq 0$ in eq. (2.27). However, our aim in this article is not to provide a detailed phenomenological fitting function, but rather to introduce the higher-order spectra in the analysis of weak lensing maps.

Extending the calculation to one loop order would allow us to include modes up to $k_\star \approx 0.3\,h\,{\rm Mpc}^{-1}$ and would significantly extend the range of validity of perturbation theory in harmonic space (e.g. up to $\ell_\star \approx 720$ at $z_s = 2$). It would thus be interesting to compute the kurt-spectra including the contribution from the one-loop matter trispectrum in the EFT framework [109–111] and compare its validity against simulations. We leave this for future work.

It is instructive to compare the problem at hand with the computation of the non-Gaussian covariance of the angular power spectrum, which takes the form [13]

$$C_{\ell\ell'} = \frac{(-1)^{\ell+\ell'}}{\sqrt{(2\ell+1)(2\ell'+1)}} T^{\ell\ell}_{\ell'\ell'}(0) - C_\ell C_{\ell'}\,. \tag{4.4}$$

[22] In general, low multipoles are affected by the finite size of the survey volume, which is more pronounced in higher-order statistics. The ray-tracing simulations inherit the finite volume corrections from the N-body simulations used to generate the lensing maps. For this reason, we have mostly concentrated on harmonics $\ell > 100$, as in the previous work [99, 108].

JCAP11(2022)020

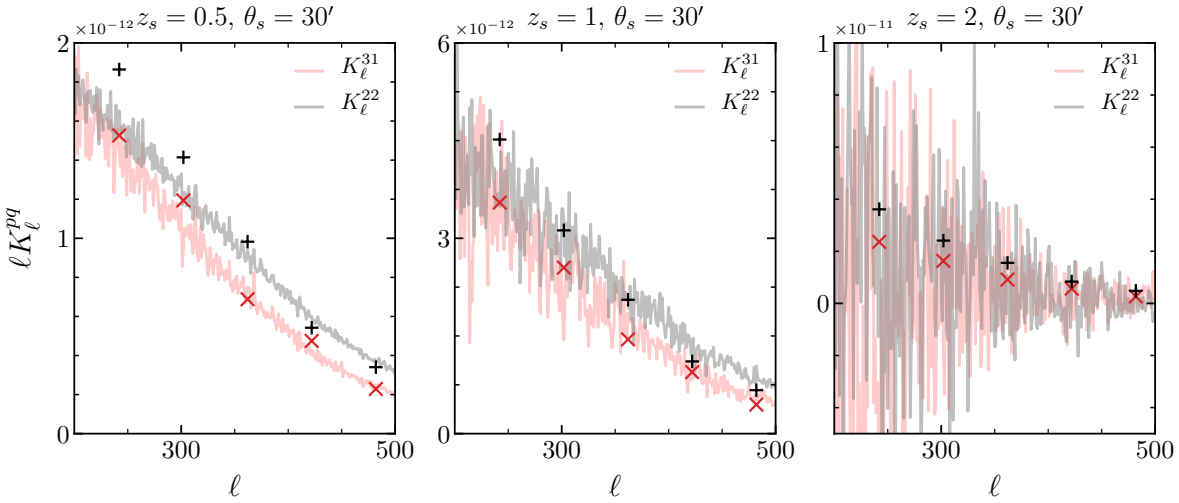

Figure 5. Comparison of theoretical and numerical results for the kurt-spectra with $\theta_s = 30'$. The discrete points represent theoretical predictions using the hierarchical ansatz. The simulation results show average of ten realisations (see text for more details).

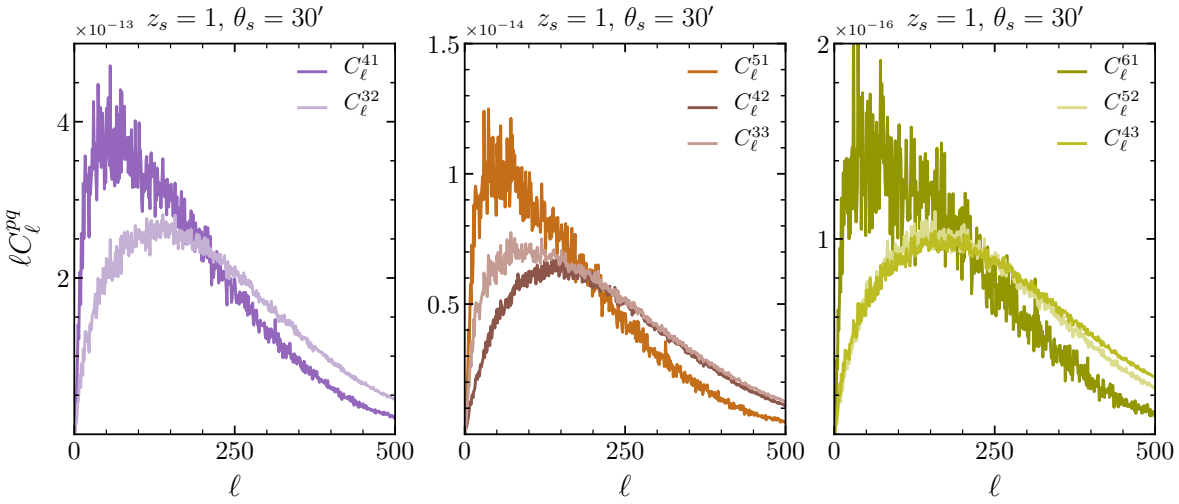

Figure 6. Higher-order spectra of weak lensing convergence at $z_s = 1$ with $\theta_s = 30'$. The different panels from left to right show the fifth-, sixth-, and seventh-order spectra.

Notice that, unlike the kurt-spectra, this does not involve summing over nonlinear modes,[23] and it is known that the tree-level approximation provides a good approximation at low multipoles [28, 86]. Moreover, the non-Gaussian covariance involves taking the infrared multipole $L = 0$, so it always receives contributions from large scales, making the HA inadequate in this case; see also [86].

4.2.4 Beyond fourth order

We have also simulated spectra beyond fourth order, as shown in figure 6. From left to right the different panels show the spectra at fifth, sixth, and seventh orders, with the smoothing

[23] Note that $T^{\ell_1\ell_2}_{\ell_3\ell_4}(L)$ is the trispectrum defined with a specific channel decomposition, so it in principle includes a sum over nonlinear modes from other channels, see (2.7). As explained earlier, these contributions are, however, usually highly suppressed in the limit $L \to 0$ and so can be neglected.

JCAP11(2022)020

scale $\theta_s = 30'$ and the source redshift $z_s = 1$. The original maps created at a `HEALPix` resolution of $N_{\rm side} = 4096$ were degraded to $N_{\rm side} = 1024$ before the analysis, and a total of ten realizations were used. All-sky maps were considered and no noise was added to the maps. The Gaussian contributions to the sixth-order spectra are also shown, while there are no Gaussian parts at odd orders.

We do not have an accurate analytical model to compute the scatter in the spectra. However, we know that the higher the power of the spectra, the more scatter it will present. This is because higher-order spectra probe the tails of the κ-distribution, so they are more susceptible to the presence (or absence) of rare high (or low) κ values. As a consequence, C_ℓ^{41} will be noisier as it contains fourth power compared to, say, C_ℓ^{32}, which cross-correlates fields with lower powers. Currently, there are no well-established estimator for higher-order non-Gaussianities beyond fourth order. Nevertheless, from the figures it is clear that surveys such as *Euclid* will be able to probe these non-Gaussian spectra beyond fourth order. Utilizing these higher-order spectra can help tighten cosmological parameter constraints.

The stage-IV weak lensing surveys will be in the signal-dominated regime [37]. Estimating the signal-to-noise involves computing the error covariance matrix of the PCL estimator that we have considered. This is nontrivial even in the context of the ordinary power spectrum in the signal dominated regime. Theoretical computation of the covariance matrix requires an analytical modeling of even high-order spectra, e.g. eight-order correlations for the covariance of the kurt-spectra estimators. This is currently not possible in a reliable manner using the HA or extensions of halo models. One possible option is to use simulations to model the higher-order correlations. Indeed, to get a reliable estimate of the off-diagonal terms in the covariance matrix, an increased number of simulations will be required. This remains an active area of research.

4.2.5 Low-ℓ modes and finite volume corrections

In the low-ℓ regime our model over predicts simulation results for both K_ℓ^{22} and K_ℓ^{31}. This is related to the fact that in this regime at least one leg of the trispectrum is in the perturbative regime. The magnitude associated with the perturbative trispectrum for a given configuration is expected to be lower than its hierarchical counterparts.

In addition, it is worth mentioning that the effect of the finite volume of the simulation is known to play an important role for the determination of one-point statistics (see, e.g., [112]). Previous studies focused on one-point moments, but the spectra we are constructing are two-point statistics. At the moment, to the best of our knowledge, there is no prescription to correct the bias due to such finite volume corrections for two-point statistics.

5 Conclusions and future prospects

Most studies of weak lensing non-Gaussianity focus on the leading-order non-Gaussianity, namely the bispectrum. In this paper, we have extended these works to fourth-order statistics by introducing two new fourth-order spectra called kurt-spectra that generalize the concept of kurtosis — the fourth-order cumulant — in harmonic space. We have used pseudo-C_ℓ-based estimators that can estimate these kurt-spectra from realistic weak-lensing maps that involve an observational mask and noise. We have shown how the Gaussian components of these spectra can be subtracted using Monte-Carlo realizations of Gaussian maps or the theoretical expectation. One of the main outcomes of our study is the fact that the kurt-spectra, as well

JCAP11(2022)020

as their higher-point generalizations, can be reliably extracted from (nearly-)all-sky weak lensing surveys.

Additionally, we have introduced a framework to compute these statistics theoretically. However, we found that obtaining an exact matching with the simulation results is not straightforward for two different reasons. At the level of the bispectrum, there currently exist halo-model-based numerical fitting functions that can be used to accurately predict the skew-spectrum. On the other hand, we do not have a such numerical fitting function for the trispectrum or beyond. In circumventing this problem, we have outlined two different (analytical) approaches in this paper based on the SPT and the HA. The SPT is only valid for large smoothing scales, while HA is expected to be valid at much smaller length scales. The kurt-spectra involve a mode sum that mixes different scales, thus underlining the case for a fitting function to reproduce the simulation results. An additional complexity is that, while computation of the skew-spectrum requires $O(\ell^2_{\rm max})$ evaluation of the bispectrum, the number of computation for the kurt-spectra is $O(\ell^3_{\rm max})$, hence restricting the resolution of maps that can be analyzed.

We have analyzed maps with $N_{\rm side} = 512$ and $\ell_{\rm max} = 1024$, and compared the simulation results with the theory predictions. With this choice, we found that the HA, despite its simplicity, can predict the general trends of the fourth-order spectra to a good accuracy in the nonlinear regime. At the same time, they show a pronounced departure from the numerical simulations at low multipole moments, due to the invalidity of the HA in this regime. We also found that the tree-level SPT trispectrum cannot be used to reliably predict the shapes of the kurt-spectra, which involve contributions from modes at $\ell \gg 100$. A better theoretical modeling is thus required to accurately compute the kurt-spectra, such as including the EFT trispectrum at one loop [109–111] in the perturbative calculation. Another possibility is to use an emulator-based approach for cosmological statistics to avoid modeling of a fitting function (see e.g. [113]).

The results presented here correspond to a single source plane. In practice, the sources are distributed over a range of redshifts, which can be easily incorporated in our modeling. Future cosmological galaxy surveys, such as the Vera Rubin Observatory, will observe a very large number of galaxies. In the absence of spectroscopic data, their redshifts will have to be inferred from the photometric redshifts (photo-z). We leave incorporating the photo-z error in our modeling and study its implications in the future.

Along with the skew-spectrum, the kurt-spectra introduced in this paper will be useful in testing various mass-mapping techniques that are generally employed. It is well known that the naive mass-mapping technique uses a flat-sky approximation known also as the Kaiser-Squires (KS) method [114], which is an inversion of the forward model in the Fourier domain. This, however, does not take into account noise or boundary effects. These are typically post-processed via convolutions that involve a large Gaussian smoothing kernel. This results in a heavy degradation of the quality of the non-Gaussian information content of high-resolution maps. In addition, there are issues related to the fact that the decomposition of spin-fields into E/B modes when performed on a bounded manifold is known to be degenerate. It is thus commonly believed that the KS estimator can perform poorly in the presence of a nontrivial mask. In recent years, a sparse hierarchical Bayesian formalism for all-sky mass-mapping without making any assumptions or impositions of Gaussianity was developed (e.g. in [115]). The estimators developed here for higher-order statistics can be used to compare the reproducibility of the non-Gaussian information in mass-mapping in the presence of a mask and noise.

JCAP11(2022)020

We have studied a few representative trispectrum configurations. Different configurations of correlation functions are associated with features in the large-scale structure, such as pancakes, filaments, clumps, voids, cosmic strings, as well as statistical anisotropy. Since the kurt-spectra reduce the entire shape information to one dimension, the study of various shapes of the trispectrum along with the kurt-spectra would thus yield a rich dividend. Based on the techniques developed in [116], an estimator that can probe individual bispectrum shapes was proposed in [108]. We plan to generalize this estimator to explore the full shape of the trispectrum in future work.

Acknowledgments

DM was supported by a grant from the Leverhulme Trust at MSSL when this project was initiated. HL and CD were partially supported by Department of Energy (DOE) grant DE-SC0020223. HL is supported by the Kavli Institute for Cosmological Physics through an endowment from the Kavli Foundation and its founder Fred Kavli. We would like to thank Peter Taylor for providing us his code to generate the Euclid-type mask used in our study. We would also like to thank Ryuichi Takahashi for making his simulations publicly available.

References

[1] J. Lesgourgues and S. Pastor, *Massive neutrinos and cosmology*, *Phys. Rept.* **429** (2006) 307 [astro-ph/0603494] [INSPIRE].

[2] H. Aihara et al., *The hyper Suprime-Cam SSP survey: overview and survey design*, *Publ. Astron. Soc. Jap.* **70** (2018) S4 [arXiv:1704.05858] [INSPIRE].

[3] DES collaboration, *Cosmology from cosmic shear with Dark Energy Survey science verification data*, *Phys. Rev. D* **94** (2016) 022001 [arXiv:1507.05552] [INSPIRE].

[4] DESI collaboration, *The DESI experiment part I. Science, targeting, and survey design*, arXiv:1611.00036 [INSPIRE].

[5] N. Tamura et al., *Prime Focus Spectrograph (PFS) for the Subaru Telescope: overview, recent progress, and future perspectives*, *Proc. SPIE Int. Soc. Opt. Eng.* **9908** (2016) 99081M [arXiv:1608.01075] [INSPIRE].

[6] K. Kuijken et al., *Gravitational lensing analysis of the kilo degree survey*, *Mon. Not. Roy. Astron. Soc.* **454** (2015) 3500 [arXiv:1507.00738] [INSPIRE].

[7] EUCLID collaboration, *Euclid definition study report*, arXiv:1110.3193 [INSPIRE].

[8] J.A. Tyson, D.M. Wittman, J.F. Hennawi and D.N. Spergel, *LSST: a complementary probe of dark energy*, *Nucl. Phys. B Proc. Suppl.* **124** (2003) 21 [astro-ph/0209632] [INSPIRE].

[9] N.R. Council, *New worlds, new horizons in astronomy and astrophysics*, The National Academies Press, Washington, DC, U.S.A. (2010).

[10] M.A. Riquelme and D.N. Spergel, *Separating the weak lensing and kinetic SZ effects from CMB temperature maps*, *Astrophys. J.* **661** (2007) 672 [astro-ph/0610007] [INSPIRE].

[11] D. Munshi, P. Valageas, L. Van Waerbeke and A. Heavens, *Cosmology with weak lensing surveys*, *Phys. Rept.* **462** (2008) 67 [astro-ph/0612667] [INSPIRE].

[12] C. Parroni, E. Tollet, V.F. Cardone, R. Maoli and R. Scaramella, *Higher-order statistics of shear field via a machine learning approach*, *Astron. Astrophys.* **645** (2021) A123 [arXiv:2011.10438] [INSPIRE].

JCAP11(2022)020

[13] W. Hu, *Angular trispectrum of the CMB*, *Phys. Rev. D* **64** (2001) 083005 [astro-ph/0105117] [INSPIRE].

[14] T. Okamoto and W. Hu, *CMB lensing reconstruction on the full sky*, *Phys. Rev. D* **67** (2003) 083002 [astro-ph/0301031] [INSPIRE].

[15] A. Cooray, C. Li and A. Melchiorri, *The trispectrum of* 21 *cm background anisotropies as a probe of primordial non-Gaussianity*, *Phys. Rev. D* **77** (2008) 103506 [arXiv:0801.3463] [INSPIRE].

[16] A. Cooray, 21 *cm background anisotropies can discern primordial non-Gaussianity*, *Phys. Rev. Lett.* **97** (2006) 261301 [astro-ph/0610257] [INSPIRE].

[17] D. Munshi, A. Heavens, A. Cooray, J. Smidt, P. Coles and P. Serra, *New optimised estimators for the primordial trispectrum*, *Mon. Not. Roy. Astron. Soc.* **412** (2011) 1993 [arXiv:0910.3693] [INSPIRE].

[18] D. Munshi, P. Coles, A. Cooray, A. Heavens and J. Smidt, *Primordial non-Gaussianity from a joint analysis of cosmic microwave background temperature and polarization*, *Mon. Not. Roy. Astron. Soc.* **410** (2011) 1295 [arXiv:1002.4998] [INSPIRE].

[19] PLANCK collaboration, *Planck* 2013 *Results. XXIV. Constraints on primordial non-Gaussianity*, *Astron. Astrophys.* **571** (2014) A24 [arXiv:1303.5084] [INSPIRE].

[20] PLANCK collaboration, *Planck* 2015 *results. XVII. Constraints on primordial non-Gaussianity*, *Astron. Astrophys.* **594** (2016) A17 [arXiv:1502.01592] [INSPIRE].

[21] PLANCK collaboration, *Planck* 2018 *results. IX. Constraints on primordial non-Gaussianity*, *Astron. Astrophys.* **641** (2020) A9 [arXiv:1905.05697] [INSPIRE].

[22] K.M. Smith, L. Senatore and M. Zaldarriaga, *Optimal analysis of the CMB trispectrum*, arXiv:1502.00635 [INSPIRE].

[23] J. Smidt et al., *A constraint on the integrated mass power spectrum out to* $z = 1100$ *from lensing of the cosmic microwave background*, *Astrophys. J. Lett.* **728** (2011) L1 [arXiv:1012.1600] [INSPIRE].

[24] PLANCK collaboration, *Planck* 2013 *results. XVII. Gravitational lensing by large-scale structure*, *Astron. Astrophys.* **571** (2014) A17 [arXiv:1303.5077] [INSPIRE].

[25] F. Bernardeau, *The large scale gravitational bias from the quasilinear regime*, *Astron. Astrophys.* **312** (1996) 11 [astro-ph/9602072] [INSPIRE].

[26] D. Munshi, A.L. Melott and P. Coles, *Generalised cumulant correlators and hierarchical clustering*, astro-ph/9812271 [INSPIRE].

[27] D. Munshi and J.D. McEwen, *Higher order spectra of weak lensing convergence maps in parametrized theories of modified gravity*, *Mon. Not. Roy. Astron. Soc.* **498** (2020) 5299 [arXiv:2004.07021] [INSPIRE].

[28] H. Lee and C. Dvorkin, *Cosmological angular trispectra and non-Gaussian covariance*, *JCAP* **05** (2020) 044 [arXiv:2001.00584] [INSPIRE].

[29] D. Gualdi, S. Novell, H. Gil-Marín and L. Verde, *Matter trispectrum: theoretical modelling and comparison to N-body simulations*, *JCAP* **01** (2021) 015 [arXiv:2009.02290] [INSPIRE].

[30] D. Bertolini, K. Schutz, M.P. Solon and K.M. Zurek, *The trispectrum in the effective field theory of large scale structure*, *JCAP* **06** (2016) 052 [arXiv:1604.01770] [INSPIRE].

[31] T. Steele and T. Baldauf, *Precise calibration of the one-loop trispectrum in the effective field theory of large scale structure*, *Phys. Rev. D* **103** (2021) 103518 [arXiv:2101.10289] [INSPIRE].

[32] A. Cooray and R.K. Sheth, *Halo models of large scale structure*, *Phys. Rept.* **372** (2002) 1 [astro-ph/0206508] [INSPIRE].

JCAP11(2022)020

[33] D. Munshi and P. Coles, *Weak lensing from strong clustering*, *Mon. Not. Roy. Astron. Soc.* **313** (2000) 148 [astro-ph/9911008] [INSPIRE].

[34] J. Alsing, T. Charnock, S. Feeney and B. Wandelt, *Fast likelihood-free cosmology with neural density estimators and active learning*, *Mon. Not. Roy. Astron. Soc.* **488** (2019) 4440 [arXiv:1903.00007] [INSPIRE].

[35] D.K. Ramanah, T. Charnock and G. Lavaux, *Painting halos from cosmic density fields of dark matter with physically motivated neural networks*, *Phys. Rev. D* **100** (2019) 043515 [arXiv:1903.10524] [INSPIRE].

[36] N. Porqueres, A. Heavens, D. Mortlock and G. Lavaux, *Lifting weak lensing degeneracies with a field-based likelihood*, *Mon. Not. Roy. Astron. Soc.* **509** (2021) 3194 [arXiv:2108.04825] [INSPIRE].

[37] P.L. Taylor, T.D. Kitching, J. Alsing, B.D. Wandelt, S.M. Feeney and J.D. McEwen, *Cosmic shear: inference from forward models*, *Phys. Rev. D* **100** (2019) 023519 [arXiv:1904.05364] [INSPIRE].

[38] A. Diaz Rivero and C. Dvorkin, *Flow-based likelihoods for non-Gaussian inference*, *Phys. Rev. D* **102** (2020) 103507 [arXiv:2007.05535] [INSPIRE].

[39] E. Allys, T. Marchand, J.-F. Cardoso, F. Villaescusa-Navarro, S. Ho and S. Mallat, *New interpretable statistics for large scale structure analysis and generation*, *Phys. Rev. D* **102** (2020) 103506 [arXiv:2006.06298] [INSPIRE].

[40] S. Mallat, *Group invariant scattering*, *Commun. Pure Appl. Math.* **65** (2012) 1331 [arXiv:1101.2286].

[41] S. Cheng, Y.-S. Ting, B. Ménard and J. Bruna, *A new approach to observational cosmology using the scattering transform*, *Mon. Not. Roy. Astron. Soc.* **499** (2020) 5902 [arXiv:2006.08561] [INSPIRE].

[42] S. Cheng and B. Ménard, *Weak lensing scattering transform: dark energy and neutrino mass sensitivity*, *Mon. Not. Roy. Astron. Soc.* **507** (2021) 1012 [arXiv:2103.09247] [INSPIRE].

[43] A.K. Saydjari, S.K.N. Portillo, Z. Slepian, S. Kahraman, B. Burkhart and D.P. Finkbeiner, *Classification of magnetohydrodynamic simulations using wavelet scattering transforms*, *Astrophys. J.* **910** (2021) 122 [arXiv:2010.11963].

[44] G. Valogiannis and C. Dvorkin, *Towards an optimal estimation of cosmological parameters with the wavelet scattering transform*, *Phys. Rev. D* **105** (2022) 103534 [arXiv:2108.07821] [INSPIRE].

[45] B. Regaldo-Saint Blancard, F. Levrier, E. Allys, E. Bellomi and F. Boulanger, *Statistical description of dust polarized emission from the diffuse interstellar medium — a RWST approach*, *Astron. Astrophys.* **642** (2020) A217 [arXiv:2007.08242] [INSPIRE].

[46] E. Allys et al., *The RWST, a comprehensive statistical description of the non-Gaussian structures in the ISM*, *Astron. Astrophys.* **629** (2019) A115 [arXiv:1905.01372] [INSPIRE].

[47] D. Munshi, P. Valageas and A.J. Barber, *Weak lensing shear and aperture-mass from linear to non-linear scales*, *Mon. Not. Roy. Astron. Soc.* **350** (2004) 77 [astro-ph/0309698] [INSPIRE].

[48] C. Uhlemann et al., *Cylinders out of a top hat: counts-in-cells for projected densities*, *Mon. Not. Roy. Astron. Soc.* **477** (2018) 2772 [arXiv:1711.04767] [INSPIRE].

[49] A. Peel, C.-A. Lin, F. Lanusse, A. Leonard, J.-L. Starck and M. Kilbinger, *Cosmological constraints with weak lensing peak counts and second-order statistics in a large-field survey*, *Astron. Astrophys.* **599** (2017) A79 [arXiv:1612.02264] [INSPIRE].

JCAP11(2022)020

[50] D. Munshi, T. Namikawa, J.D. McEwen, T.D. Kitching and F.R. Bouchet, *Morphology of weak lensing convergence maps*, *Mon. Not. Roy. Astron. Soc.* **507** (2021) 1421 [arXiv:2010.05669] [INSPIRE].

[51] C.-T. Chiang, C. Wagner, A.G. Sánchez, F. Schmidt and E. Komatsu, *Position-dependent correlation function from the SDSS-III baryon oscillation spectroscopic survey data release* 10 *CMASS sample*, *JCAP* **09** (2015) 028 [arXiv:1504.03322] [INSPIRE].

[52] M.J. Drinkwater et al., *The WiggleZ dark energy survey: survey design and first data release*, *Mon. Not. Roy. Astron. Soc.* **401** (2010) 1429 [arXiv:0911.4246] [INSPIRE].

[53] V. Desjacques, D. Jeong and F. Schmidt, *Large-scale galaxy bias*, *Phys. Rept.* **733** (2018) 1 [arXiv:1611.09787] [INSPIRE].

[54] E. Mitsou, J. Yoo, R. Durrer, F. Scaccabarozzi and V. Tansella, *General and consistent statistics for cosmological observations*, *Phys. Rev. Res.* **2** (2020) 033004 [arXiv:1905.01293] [INSPIRE].

[55] D.M. Regan, E.P.S. Shellard and J.R. Fergusson, *General CMB and primordial trispectrum estimation*, *Phys. Rev. D* **82** (2010) 023520 [arXiv:1004.2915] [INSPIRE].

[56] M. Levi and Z. Vlah, *Massive neutrinos in nonlinear large scale structure: a consistent perturbation theory*, arXiv:1605.09417 [INSPIRE].

[57] S.-F. Chen, H. Lee and C. Dvorkin, *Precise and accurate cosmology with CMB×LSS power spectra and bispectra*, *JCAP* **05** (2021) 030 [arXiv:2103.01229] [INSPIRE].

[58] T. Matsubara, *Analytic Minkowski functionals of the cosmic microwave background: second-order non-Gaussianity with bispectrum and trispectrum*, *Phys. Rev. D* **81** (2010) 083505 [arXiv:1001.2321] [INSPIRE].

[59] D. Munshi, B. Hu, T. Matsubara, P. Coles and A. Heavens, *Lensing-induced morphology changes in CMB temperature maps in modified gravity theories*, *JCAP* **04** (2016) 056 [arXiv:1602.00965] [INSPIRE].

[60] V. Assassi, M. Simonović and M. Zaldarriaga, *Efficient evaluation of angular power spectra and bispectra*, *JCAP* **11** (2017) 054 [arXiv:1705.05022] [INSPIRE].

[61] H.S. Grasshorn Gebhardt and D. Jeong, *Fast and accurate computation of projected two-point functions*, *Phys. Rev. D* **97** (2018) 023504 [arXiv:1709.02401] [INSPIRE].

[62] N. Schöneberg, M. Simonović, J. Lesgourgues and M. Zaldarriaga, *Beyond the traditional line-of-sight approach of cosmological angular statistics*, *JCAP* **10** (2018) 047 [arXiv:1807.09540] [INSPIRE].

[63] A.J.S. Hamilton, *Uncorrelated modes of the nonlinear power spectrum*, *Mon. Not. Roy. Astron. Soc.* **312** (2000) 257 [astro-ph/9905191] [INSPIRE].

[64] B. Leistedt and J.D. McEwen, *Exact wavelets on the ball*, *IEEE Trans. Signal. Process.* **60** (2012) 6257 [arXiv:1205.0792] [INSPIRE].

[65] J.E. Campagne, J. Neveu and S. Plaszczynski, *Angpow: a software for the fast computation of accurate tomographic power spectra*, *Astron. Astrophys.* **602** (2017) A72 [arXiv:1701.03592] [INSPIRE].

[66] Z. Slepian, *On decoupling the integrals of cosmological perturbation theory*, *Mon. Not. Roy. Astron. Soc.* **507** (2021) 1337 [arXiv:1812.02728] [INSPIRE].

[67] E. Di Dio, R. Durrer, R. Maartens, F. Montanari and O. Umeh, *The full-sky angular bispectrum in redshift space*, *JCAP* **04** (2019) 053 [arXiv:1812.09297] [INSPIRE].

[68] X. Fang, E. Krause, T. Eifler and N. MacCrann, *Beyond Limber: efficient computation of angular power spectra for galaxy clustering and weak lensing*, *JCAP* **05** (2020) 010 [arXiv:1911.11947] [INSPIRE].

JCAP11(2022)020

[69] A.C. Deshpande and T.D. Kitching, *Post-Limber weak lensing bispectrum, reduced shear correction, and magnification bias correction*, *Phys. Rev. D* **101** (2020) 103531 [arXiv:2004.01666] [INSPIRE].

[70] H.S. Grasshorn Gebhardt and D. Jeong, *Nonlinear redshift-space distortions in the harmonic-space galaxy power spectrum*, *Phys. Rev. D* **102** (2020) 083521 [arXiv:2008.08706] [INSPIRE].

[71] X. Fang, T. Eifler and E. Krause, *2D-FFTLog: efficient computation of real space covariance matrices for galaxy clustering and weak lensing*, *Mon. Not. Roy. Astron. Soc.* **497** (2020) 2699 [arXiv:2004.04833] [INSPIRE].

[72] F. Montanari and S. Camera, *Speeding up the detectability of the harmonic-space galaxy bispectrum*, *JCAP* **01** (2021) 002 [arXiv:2008.11131] [INSPIRE].

[73] O. Umeh, *Optimal computation of anisotropic galaxy three point correlation function multipoles using 2DFFTLOG formalism*, *JCAP* **05** (2021) 035 [arXiv:2011.05889] [INSPIRE].

[74] D.N. Limber, *The analysis of counts of the extragalactic nebulae in terms of a fluctuating density field. II*, *Astrophys. J.* **119** (1954) 655 [INSPIRE].

[75] M. LoVerde and N. Afshordi, *Extended Limber approximation*, *Phys. Rev. D* **78** (2008) 123506 [arXiv:0809.5112] [INSPIRE].

[76] F. Bernardeau, S. Colombi, E. Gaztanaga and R. Scoccimarro, *Large scale structure of the universe and cosmological perturbation theory*, *Phys. Rept.* **367** (2002) 1 [astro-ph/0112551] [INSPIRE].

[77] M.H. Goroff, B. Grinstein, S.J. Rey and M.B. Wise, *Coupling of modes of cosmological mass density fluctuations*, *Astrophys. J.* **311** (1986) 6 [INSPIRE].

[78] B. Jain and E. Bertschinger, *Second order power spectrum and nonlinear evolution at high redshift*, *Astrophys. J.* **431** (1994) 495 [astro-ph/9311070] [INSPIRE].

[79] H. Gil-Marin, C. Wagner, F. Fragkoudi, R. Jimenez and L. Verde, *An improved fitting formula for the dark matter bispectrum*, *JCAP* **02** (2012) 047 [arXiv:1111.4477] [INSPIRE].

[80] D. Gualdi, H.e. Gil-Marín and L. Verde, *Joint analysis of anisotropic power spectrum, bispectrum and trispectrum: application to N-body simulations*, *JCAP* **07** (2021) 008 [arXiv:2104.03976] [INSPIRE].

[81] J.N. Fry, *The galaxy correlation hierarchy in perturbation theory*, *Astrophys. J.* **279** (1984) 499 [INSPIRE].

[82] J.N. Fry and P.J.E. Peebles, *Statistical analysis of catalogs of extragalactic objects. IX. The four-point galaxy correlation function*, *Astrophys. J.* **221** (1978) 19.

[83] F. Bernardeau and R. Schaeffer, *Halo correlations in nonlinear cosmic density fields*, *Astron. Astrophys.* **349** (1999) 697 [astro-ph/9903387] [INSPIRE].

[84] F. Bernardeau and R. Schaeffer, *Galaxy correlations, matter correlations and biasing*, *Astron. Astrophys.* **255** (1992) 1.

[85] P. Coles, A. Melott and D. Munshi, *Bias and hierarchical clustering*, *Astrophys. J. Lett.* **521** (1999) L5 [astro-ph/9904253] [INSPIRE].

[86] R. Scoccimarro, M. Zaldarriaga and L. Hui, *Power spectrum correlations induced by nonlinear clustering*, *Astrophys. J.* **527** (1999) 1 [astro-ph/9901099] [INSPIRE].

[87] I. Szapudi and A.S. Szalay, *Higher order statistics of the galaxy distribution using generating functions*, *Astrophys. J.* **408** (1993) 43.

[88] P. Boschan, I. Szapudi and A.S. Szalay, *On the accurate determination of the clustering hierarchy of galaxies*, *Astrophys. J. Suppl.* **93** (1994) 65.

JCAP11(2022)020

[89] F. Bernardeau and R. Schaeffer, *Halo correlations in nonlinear cosmic density fields*, *Astron. Astrophys.* **349** (1999) 697 [astro-ph/9903387] [INSPIRE].

[90] D. Munshi and B. Jain, *The statistics of weak lensing at small angular scales: probability distribution function*, *Mon. Not. Roy. Astron. Soc.* **318** (2000) 109 [astro-ph/9911502] [INSPIRE].

[91] D. Munshi and B. Jain, *Statistics of weak lensing at small angular scales: analytical predictions for lower order moments*, *Mon. Not. Roy. Astron. Soc.* **322** (2001) 107 [astro-ph/9912330] [INSPIRE].

[92] A.J. Barber, D. Munshi and P. Valageas, *From linear to nonlinear scales: analytical and numerical predictions for the weak lensing convergence*, *Mon. Not. Roy. Astron. Soc.* **347** (2004) 667 [astro-ph/0304451] [INSPIRE].

[93] S. Colombi, *A 'skewed' lognormal approximation to the probability distribution function of the large scale density field*, *Astrophys. J. Lett.* **435** (1994) L536 [astro-ph/9402071] [INSPIRE].

[94] O.H.E. Philcox, D.N. Spergel and F. Villaescusa-Navarro, *Effective halo model: creating a physical and accurate model of the matter power spectrum and cluster counts*, *Phys. Rev. D* **101** (2020) 123520 [arXiv:2004.09515] [INSPIRE].

[95] R. Takahashi et al., *Fitting the nonlinear matter bispectrum by the halofit approach*, *Astrophys. J.* **895** (2020) 113 [arXiv:1911.07886] [INSPIRE].

[96] A. Lewis, *The real shape of non-Gaussianities*, *JCAP* **10** (2011) 026 [arXiv:1107.5431] [INSPIRE].

[97] D. Munshi et al., *The weak lensing bispectrum induced by gravity*, *Mon. Not. Roy. Astron. Soc.* **493** (2020) 3985 [arXiv:1910.04627] [INSPIRE].

[98] T. Fujita and Z. Vlah, *Perturbative description of biased tracers using consistency relations of LSS*, *JCAP* **10** (2020) 059 [arXiv:2003.10114] [INSPIRE].

[99] D. Munshi, T. Namikawa, T.D. Kitching, J.D. McEwen and F.R. Bouchet, *Weak lensing skew-spectrum*, *Mon. Not. Roy. Astron. Soc.* **498** (2020) 6057 [arXiv:2006.12832] [INSPIRE].

[100] M. Schmittfull, T. Baldauf and U. Seljak, *Near optimal bispectrum estimators for large-scale structure*, *Phys. Rev. D* **91** (2015) 043530 [arXiv:1411.6595] [INSPIRE].

[101] A. Moradinezhad Dizgah, H. Lee, M. Schmittfull and C. Dvorkin, *Capturing non-Gaussianity of the large-scale structure with weighted skew-spectra*, *JCAP* **04** (2020) 011 [arXiv:1911.05763] [INSPIRE].

[102] M. Schmittfull and A. Moradinezhad Dizgah, *Galaxy skew-spectra in redshift-space*, *JCAP* **03** (2021) 020 [arXiv:2010.14267] [INSPIRE].

[103] R. Takahashi et al., *Full-sky gravitational lensing simulation for large-area galaxy surveys and cosmic microwave background experiments*, *Astrophys. J.* **850** (2017) 24 [arXiv:1706.01472] [INSPIRE].

[104] D. Munshi, T. Namikawa, T.D. Kitching, J.D. McEwen and F.R. Bouchet, *Weak lensing skew-spectrum*, *Mon. Not. Roy. Astron. Soc.* **498** (2020) 6057 [arXiv:2006.12832] [INSPIRE].

[105] K.M. Górski et al., *HEALPix — a framework for high resolution discretization, and fast analysis of data distributed on the sphere*, *Astrophys. J.* **622** (2005) 759 [astro-ph/0409513] [INSPIRE].

JCAP11(2022)020

[106] E. Hivon, K.M. Gorski, C.B. Netterfield, B.P. Crill, S. Prunet and F. Hansen, *Master of the cosmic microwave background anisotropy power spectrum: a fast method for statistical analysis of large and complex cosmic microwave background data sets*, *Astrophys. J.* **567** (2002) 2 [astro-ph/0105302] [INSPIRE].

[107] C. Hikage, M. Takada, T. Hamana and D. Spergel, *Shear power spectrum reconstruction using pseudo-spectrum method*, *Mon. Not. Roy. Astron. Soc.* **412** (2011) 65 [arXiv:1004.3542] [INSPIRE].

[108] D. Munshi et al., *The weak lensing bispectrum induced by gravity*, *Mon. Not. Roy. Astron. Soc.* **493** (2020) 3985 [arXiv:1910.04627] [INSPIRE].

[109] D. Bertolini, K. Schutz, M.P. Solon, J.R. Walsh and K.M. Zurek, *Non-Gaussian covariance of the matter power spectrum in the effective field theory of large scale structure*, *Phys. Rev. D* **93** (2016) 123505 [arXiv:1512.07630] [INSPIRE].

[110] D. Bertolini, K. Schutz, M.P. Solon and K.M. Zurek, *The trispectrum in the effective field theory of large scale structure*, *JCAP* **06** (2016) 052 [arXiv:1604.01770] [INSPIRE].

[111] T. Steele and T. Baldauf, *Precise calibration of the one-loop trispectrum in the effective field theory of large scale structure*, *Phys. Rev. D* **103** (2021) 103518 [arXiv:2101.10289] [INSPIRE].

[112] I. Szapudi and S. Colombi, *Cosmic error and the statistics of large scale structure*, *Astrophys. J.* **470** (1996) 131 [astro-ph/9510030] [INSPIRE].

[113] A. Spurio Mancini, D. Piras, J. Alsing, B. Joachimi and M.P. Hobson, *CosmoPower: emulating cosmological power spectra for accelerated Bayesian inference from next-generation surveys*, *Mon. Not. Roy. Astron. Soc.* **511** (2022) 1771 [arXiv:2106.03846] [INSPIRE].

[114] N. Kaiser and G. Squires, *Mapping the dark matter with weak gravitational lensing*, *Astrophys. J.* **404** (1993) 441 [INSPIRE].

[115] M.A. Price, J.D. Mcewen, L. Pratley and T.D. Kitching, *Sparse Bayesian mass-mapping with uncertainties: full sky observations on the celestial sphere*, *Mon. Not. Roy. Astron. Soc.* **500** (2020) 5436 [arXiv:2004.07855] [INSPIRE].

[116] T. Namikawa, B. Bose, F.R. Bouchet, R. Takahashi and A. Taruya, *CMB lensing bispectrum: assessing analytical predictions against full-sky lensing simulations*, *Phys. Rev. D* **99** (2019) 063511 [arXiv:1812.10635] [INSPIRE].

JCAP11(2022)020